THESIS

INTERNET OF THINGS MONITORING OF THE OXIDATION REDUCTION POTENTIAL IN AN OLEOPHILIC BIO-BARRIER

Submitted by

Wesley W Hogan

Department of Civil and Environmental Engineering

In partial fulfillment of the requirements

for the Degree of Master of Science

Colorado State University

Fort Collins, Colorado

Summer 2020

Master's Committee:

Advisor: Dr. Joseph Scalia
Co-Advisor: Dr. Thomas Sale

Dr. Jay Ham

ABSTRACT

INTERNET OF THINGS MONITORING OF THE OXIDATION REDUCTION POTENTIAL IN AN OLEOPHILIC BIO-BARRIER

Petroleum hydrocarbons discharged to surface water at a groundwater-surface water interface (GSI) resulting in violations of the Clean Water Act often spark costly cleanup efforts. The oleophilic bio-barrier (OBB) has been shown to be effective in catching and retaining oils via an oleophilic (oil-loving) geocomposite and facilitating biodegradation through cyclic delivery of oxygen and nutrients via tidally driven water level fluctuations. Conventional resistive (e.g., geomembrane) or absorptive-only (e.g., organoclay) barriers for oil at GSIs limit oxygen diffusion into underlying sediments and are susceptible to overloading and bypass. Conversely, OBBs are designed to function as sustainable oil-degrading bioreactors. For an OBB to be effective, the barrier must maintain aerobic conditions created by tidally driven oxygen delivery. Oxidation reduction potential (ORP) sensors were installed within an OBB in the northeastern US with an internet of things (IoT) monitoring system to either confirm the sustained oxidizing conditions within the OBB, or to detect a problem within the OBB and trigger additional remedial action. Real-time ORP data revealed consistently aerobic oxidation-reduction (redox) conditions within the OBB with periods of slightly less oxidized redox conditions in response to precipitation. By interpreting ORP data in real time, we were able to verify that the OBB maintained the oxidizing conditions critical to the barrier functioning as an effective aerobic bioreactor to degrade potentially-sheen generating oils at GSIs. In

addition, alternative oleophilic materials were tested to increase the range of candidate materials that may function as the oleophilic component of an OBB. Materials tested included thin black (232 g/m^2), thin white (244 g/m^2), medium black (380 g/m^2), and thick black (1055 g/m^2) geotextiles, as well as a coconut fiber coir mat. Finally, a model was developed to estimate the required sorptive capacity of the oleophilic component of an OBB based on site-specific conditions, which can be used to inform OBB design.

ACKNOWLEDGEMENTS

I would like to thank the following people for their support and encouragement:

- Dr. Joe Scalia for the opportunity to work on a project that I very much enjoyed as well as his support and guidance throughout my degree
- Dr. Tom Sale for his expertise and guidance regarding OBBs and ORP monitoring
- Dr. Jay Ham for serving on my committee
- Zach Ferrie for his expertise and guidance regarding coding and sensors
- Kayvan Karimi for his help with data visualization
- Sam Gallo for his IoT sensor expertise
- Maria Irianni Renno for her microbiology expertise and guidance in the lab
- Alison Hawkins, Marc Chalfant, Calista Campbell, Laura Tochko, Nate Jacobs and all the other previous students whose work has advanced the knowledge of sheens and OBBs
- My fellow colleagues at the Center for Contaminant Hydrology who helped with everything from classwork to practice presentations
- My family and friends for their love and support

Funding was provided by Chevron Energy Technology Company.

TABLE OF CONTENTS

LIST OF TABLES

LIST OF FIGURES

1. INTRODUCTION

1.1. Problem Statement

Petroleum hydrocarbons from historic upland releases near surface waters, often resulting from historic petroleum refining, distribution, or storage facilities near waterways, continue to be a major environmental concern. As oils are discharged to surface water at a groundwater-surface water interface (GSI), resulting sheens, a violation of the Clean Water Act, often spark costly cleanup efforts. Natural attenuation processes are an integral factor in the depletion of oil in the subsurface and can stabilize a plume given adequate sorption and degradation rates. However, when sorption and natural attenuation are insufficient in stopping the flow of oil into surface water, additional actions including upland source zone control, and containment at the GSI are often necessary.

Over the past decade, Chevron Energy Technology Company has funded four students (Hawkins 2013; Chalfant 2015; Campbell 2017; Tochko 2018) of the Center for Contaminant Hydrology at Colorado State University to study sheen formation and develop sustainable solutions that are practical and cost effective. This thesis follows these previous efforts through additional lab and field studies focused on deepening our knowledge of a technology developed through this collaboration termed oleophilic bio-barriers (OBBs) (Zimbron et al. 2014; US Patent Number US20160075576A1).

Oxidation reduction potential (ORP) sensors with IoT capabilities have been used to monitor oxidation-reduction (redox) conditions and characterize a contaminated site in real time. IoT connected ORP sensors can be used to gauge if an OBB is maintaining the geochemical conditions foundational to functioning as an effective and sustainable

bioreactor and to send an alert when conditions in an OBB behave unexpectedly (e.g. sustained anaerobic conditions due to sediment accumulation limiting oxygen ingress). If data are interpreted to indicate a malfunction in the OBB, the alert system will have provided valuable time to act before failure occurs as the sorptive capacity of the OBB is reached. Therefore, measuring ORP continuously within an OBB is expected to be beneficial for site monitoring and building trust that the system is functioning as expected, as well as refining our understanding of the geochemistry within an OBB.

1.2. Objectives

The primary objective of this study is to improve our effective use of OBBs. To accomplish this objective, an IoT ORP monitoring system was developed and used to verify the sustained oxidizing conditions within an OBB. Our hope is that providing proof of concept of a real-time OBB monitoring system will furnish remedial decision makers with a tool that will help further their understanding of site specific conditions, demonstrate continued efficacy, and ultimately improve decision making. Two experiments were conducted to provide proof of concept for an IoT ORP monitoring system. The first was a laboratory scale OBB sand tank experiment, where ORP sensors were installed in an OBB and water levels were fluctuated to simulate a tidal environment (further discussed in Chapter 4). The sensors were arranged to observe oxygen delivery to the system in response to changing water levels, as well as to observe the extent of oxygen diffusion into the OBB. In the second experiment, ORP sensors were installed in a field scale OBB protective cap overlaying oil-impacted media that has been loaded by historical upland oil releases that have since been remediated (further discussed in Chapter 3). The field

OBB was installed at a GSI in a tidal zone, and an IoT sensor system was installed in the OBB to record and report ORP data.

Because the sorption capacity of an OBB is a critical design detail to prevent overloading of the system as the aerobic microbiome initially comes online, or in the case of sediment fouling before repair actions can be taken, we evaluated the oil retention capacities of alternative oleophilic candidate materials. Material sorption capacity was characterized by submerging materials in diesel or crude oil, as well as loading materials with diesel while suspended in water. Finally, we estimated the oil degradation rate within an OBB to develop a preliminary model for the required sorption capacity of an OBB given different site-specific variables such as OBB redox conditions and oil loading rates.

2. BACKGROUND

2.1. Oleophilic Bio-Barriers

Oleophilic bio-barriers have been shown to be effective in catching and retaining oil at a GSI, as well as facilitating biodegradation (Zimbron et al. 2014; Chalfant 2015; Campbell 2017; Tochko 2018). An OBB is conceptually illustrated in Figure 1 and is composed of a geocomposite drainage layer (GDL) consisting of a geonet sandwiched between two oleophilic (oil-loving) non-woven geotextiles as shown in Figure 2. Generally, an OBB includes an overlying layer of clean sand fill to act as a capillary barrier to further prevent oil from migrating upward and out of the GDL. An additional geotextile layer is often installed above the sand layer to limit sedimentation into the overlying sand and GDL and to protect underlying layers from the overlying structural cover (e.g. riprap). The structural cover anchors the OBB in place and provides protection against

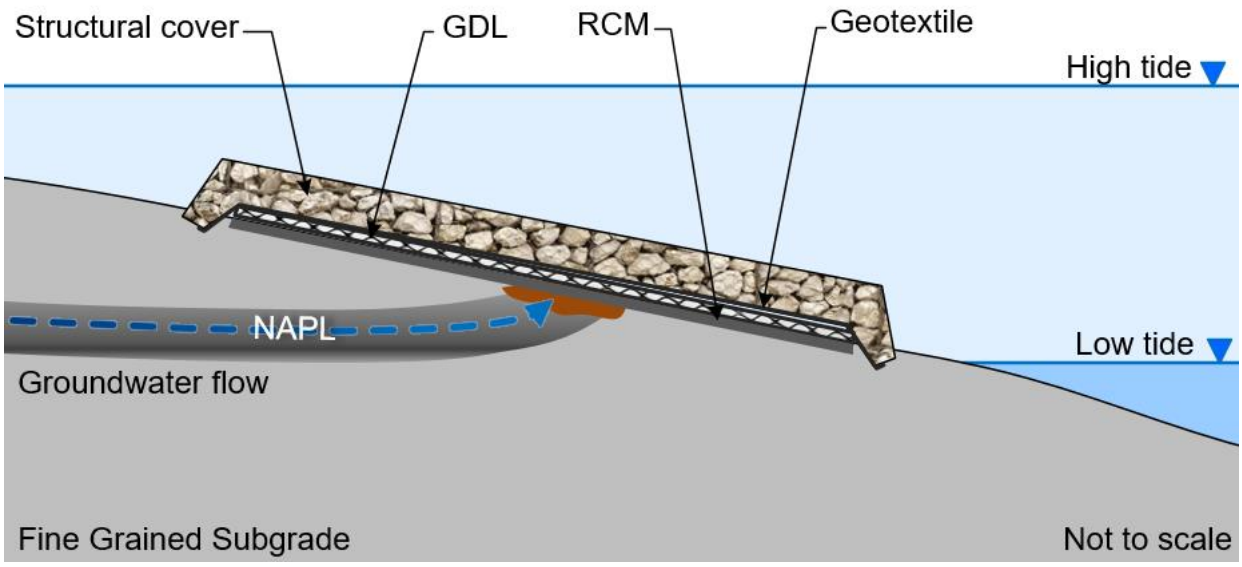

Figure 1. Oleophilic bio-barrier conceptual diagram.

bank erosion, wave action, and ice scour. Overall, the OBB has proven to be an effective sheen remedy that offers a simple installation, low capital and operation and maintenance costs, and promising long-term performance (Tochko 2018).

Oleophilic bio-barriers are placed at a GSI, as shown in Figure 1, to prevent oil migrating on top of the groundwater table from contaminating surface water via seeps, ebullition, and erosion (Sale et al. 2018). As oil migrates through the OBB, the oil spontaneously imbibes to the high surface area oleophilic geotextile component of the GDL and is retained. Concurrently, tidally driven water level fluctuations deliver oxygen and nutrients via the geonet component of the GDL to the geotextiles and surrounding sediments (Tochko 2018). The increased nutrient availability decreases the likelihood that

Figure 2. Photo of a geocomposite drainage layer during OBB installation.

microbial metabolism is nutrient limited. The increased supply of oxygen to the system results in a more oxidized environment, and ideally achieves and maintains aerobic conditions. Aerobic conditions are critical to ensuring rapid degradation of oil that reaches the OBB such that oil reaching the OBB does not exceed the retention capacity of the oleophilic component(s). Oil degrades most efficiently in oxidized environments, but degradation efficiency decreases as conditions become more reduced (Das and Chandran 2011).

Oil adsorptive barriers such as absorptive media (e.g. organoclay) barriers often limit oxygen diffusion into the underlying soil, creating a more reducing environment less suitable for oil degradation, forcing the barrier to rely on a finite retention capacity (Chalfant 2015; Tochko 2018). The ability of an OBB to enhance oil degradation addresses concerns that hinder traditional physical containment and adsorptive barriers. Cost effectiveness is another benefit of OBBs as initial capital and operation and maintenance costs are less than alternative sheen remedies (Chalfant 2015). This combination of cost effectiveness and sustainability make OBBs an appealing solution for oil containment at GSIs.

2.2. Oxidation Reduction Potential

Oxidation reduction potential (ORP) is a thermodynamic parameter which describes the activity of an aqueous environment or a soil (Striggow 2017). Soil ORP values are obtained by measuring the difference in voltage (Eh) between a reference electrode and a sensing electrode (Fiedler et al. 2007). Reference electrodes have a stable and well-known redox potential that is used to measure ORP against a sensing

electrode. To effectively measure the soil ORP, both electrodes must have a continuous hydraulic connection to serve as an ion junction (Fiedler et al. 2007).

Redox reactions require both an electron donor and acceptor for the chemical reaction to occur. Oxidation occurs when an atom loses an electron and reduction occurs when an atom gains an electron. Each chemical species has an ORP where a more positive (or more oxidized) ORP indicates a greater affinity for electrons, and a more negative (or more reduced) ORP indicates the chemical species is more inclined to discard electrons (VanLoon and Duffy 2011). Common chemical reaction electron acceptors and donors are known as redox couples. A redox ladder is a hierarchy of redox reactions organized from most oxidized at the top to least oxidized on the bottom. A redox ladder relevant to how ORP data is interpreted for OBB monitoring purposes is provided in Figure 3, where each step on the redox ladder represents a redox couple with the oxidized species on the top and the reduced species on the bottom. The color scale used in Figure 3 ranges from purple at a -619 mV ORP (rgb 102,0,255) to red at a 611 mV ORP (rgb 204,0,0). Figure 3 also correlates these soil redox couples to ORP (mV) for a silver-silver chloride (Ag-AgCl) or a palladium-palladium chloride (Pd-$PdCl_2$) reference electrode. These relationships can be used to infer which dominant electron acceptors and donors are present in the system.

In an oil impacted sediment, the carbon rich oil is the dominant electron donor barring the presence of a more energy abundant substrate (Abbasian et al. 2015). When completely degraded, oil is oxidized to methane, carbon dioxide, and water (Varjani, 2017). In terms of complete mineralization, oil is known to be most readily degraded under aerobic conditions (Das and Chandran 2011) as anaerobic microorganisms tend to exhibit

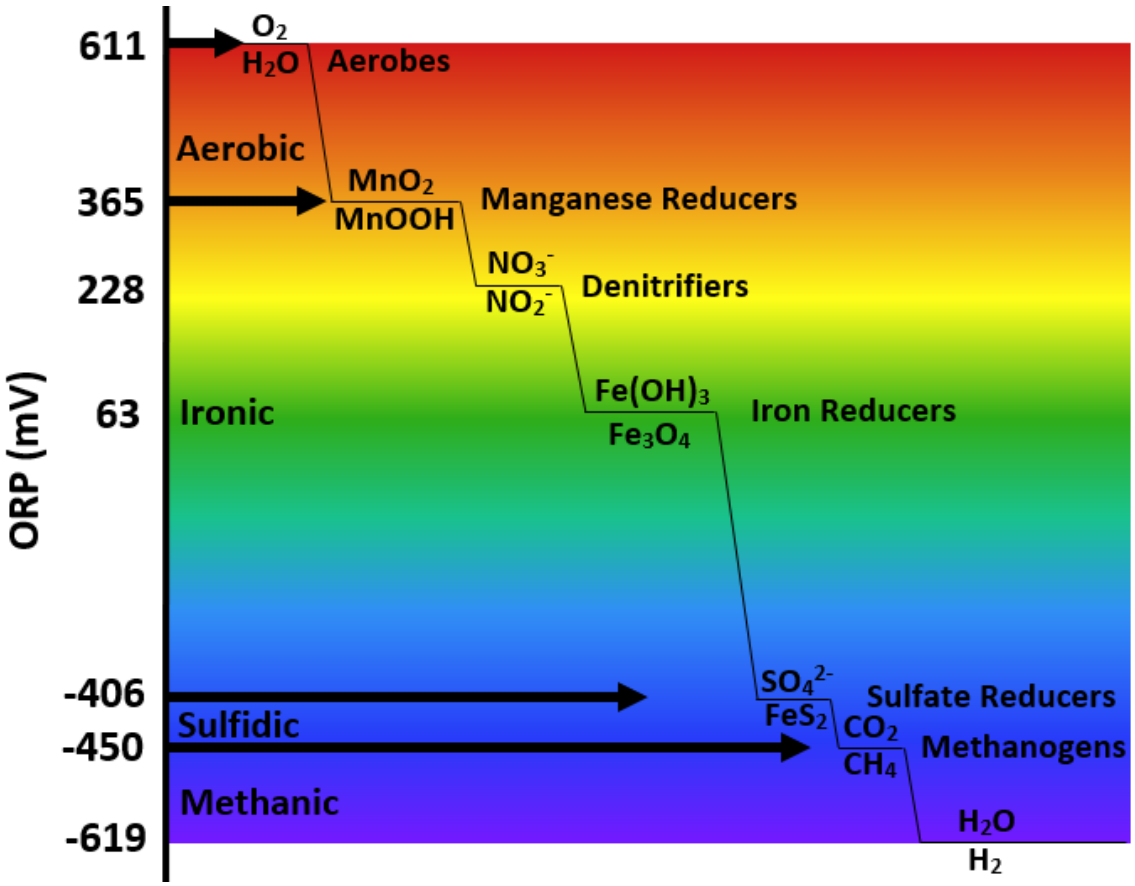

Figure 3. Redox ladder with corresponding ORP values [color scale ranges from purple at a -619 mV ORP (rgb 102,0,255) to red at a 611 mV ORP(rgb 204,0,0)] (after Vilgalys 2012; Sale 2020).

much slower growth than their aerobic counterparts (Hinchee and Olfenbuttel 2013; Widdel et al. 2006). Based on thermodynamics, the electron acceptors from most energetically preferred to least preferred by soil microbial communities are oxygen, manganese (IV), nitrate, nitrite, iron (III), sulfate, and carbon dioxide (Essington 2015). This sequence is also the order in which the electron acceptors are preferred for oil biodegradation (Brauner and Widdowson 1997). Oil degradation efficiency is related to the available electron acceptors, and the degradation efficiency increases with more favorable electron acceptors. For example, oil will be degraded more quickly when

Iron(III) is available for microbial uptake than when carbon dioxide is the only available electron acceptor (Das and Chandran 2011).

ORP values reflect site specific characteristics such as pH, soil organic matter, salinity, and temperature. For example, microbial activity and ORP increase as temperatures rise, and oil is known to degrade more quickly at higher temperatures (Atlas 1981). Moreover, changes in pH inversely affect ORP as governed by the Nernst equation. Commonly, a correction of -59 mV per pH unit at 25 °C is used, but studies have shown that this ORP correction can vary from -6 mV to -256 mV per unit pH in different environments (Fiedler et al. 2007).

2.3. Oil at Groundwater-Surface Water Interfaces

Due to historical oil releases, contaminated sediments and groundwater can discharge oil into nearby surface waters at the GSI, creating iridescent sheens as shown in Figure 4. Releases of oil at GSIs occur through seeps, ebullition, and erosion (Sale et al. 2018). Seeps generally occur as water levels decrease through preferential flow paths in the porous media. Ebullition describes the process in which the degradation products carbon dioxide and methane in subsurface media form gas bubbles that rise up through the GSI via buoyant forces and burst on the water surface. These gas bubbles have water as the wetting fluid, gas as the non-wetting fluid, and may contain oil as the intermediate wetting fluid. When the bubbles reach the water surface, the gas is released into the atmosphere, and the oil spreads across the surface water as a sheen. Finally, when erosion occurs in contaminated sediments, oil trapped within the subsurface may be released into surface water and form sheens.

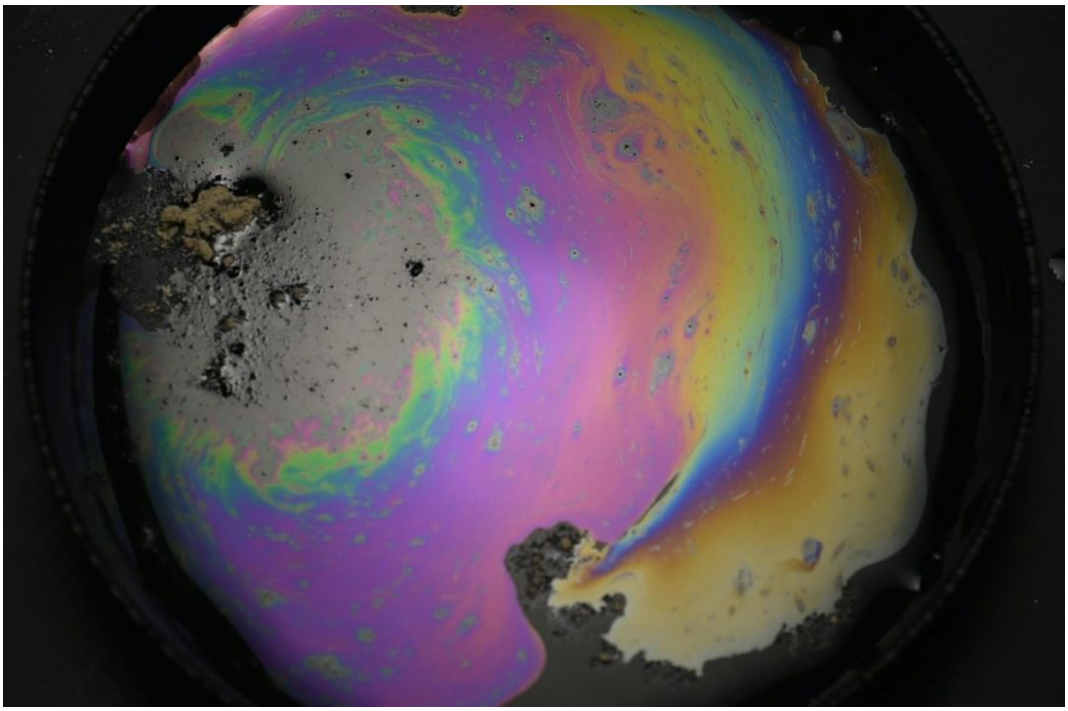

Figure 4. Photo of an oil (crude oil) sheen (Sitler 2020).

Groundwater-surface water interfaces offer unique environments for oil degradation. Tidal fluctuations can cause dramatic changes in soil chemistry, such as drastic shifts in ORP within hours or even minutes. Water table fluctuations also create a smear zone that spreads oil over a greater volume, which enlarges the volume of a plume, but also increases the magnitude of biodegradation by exposing the oil to more microbes, nutrients, and electron acceptors (Yadav and Hassanizadeh 2011).

For sediments that experience groundwater table fluctuation in response to tidal fluctuation, there are generally three microbial zones within the subsurface: the oxic zone, which is located near the surface above high tide, the reduced zone, located below the capillary fringe at low tide, and the suboxic or smear zone (herein referred to as the transition zone), which is between the oxic and reduced zones (Reddy and DeLaune 2008). Oxidizing microbes thrive in aerobic zones with an aerobic ORP (> 365 mV).

Strongly reducing microbes thrive in anaerobic zones with an ORP correlated with the sulfidic or methanic redox couple (< -406 mV) (Reddy and DeLaune 2008; Sale 2020). Moderately reducing microbes thrive in transition zones with an ORP (between -406 mV and 365 mV), but depending on site-specific conditions, the transition zone can also be suitable for either or both oxidizing and strongly reducing microbes. Microbial communities present in transition zones have also been shown to adjust to regularly changing soil conditions so they can modify their metabolism to use different electron acceptors based on the redox conditions at a given time (DeAngelis et al. 2010).

Water table fluctuations have been shown to increase microbial activity in transition zones by combined degradation of reducing microbes during flooded (reducing) periods and oxidizing microbes during drained (oxidizing) periods (Banks et al. 1999; Dobson et al. 2007). For an OBB at a tidal GSI, nutrient rich oxygenated surface water floods the OBB. During flooded periods, the most favorable electron acceptor is consumed by microbes until that electron acceptor is no longer available, and the next most favorable electron acceptor is then used. High tide can benefit dryer upper bank sediments because the short flooded period allows the soil to sustain a sufficient moisture content for microbial growth (Yadav and Hassanizadeh 2011). When the tide falls, atmospheric oxygen diffuses into the sediment and OBB. The cyclical oxygen delivery enhances microbial metabolism and sets off a cascade of redox reactions where oxygen is used as an electron acceptor either to directly oxidize oil or to oxidize reduced soil species such as manganite or magnetite to oxidized states. These oxidized soil species are then used as an electron acceptor to oxidize oil, where they are converted back to the reduced state, and the cycle begins again.

3. FIELD OLEOPHILIC BIO-BARRIER MONITORING

3.1. Introduction

A former oil import/export terminal located adjacent to a tidally fluctuating GSI in the northeastern United States had historic oil releases from an upland tank farm that contaminated subsurface sediments. Although upland subsurface contamination has been remediated, there is still concern that the transport of oil may result in the formation of sheens on the water surface. To prevent sheening, an OBB was installed to catch, retain, and degrade oil at the GSI. The OBB installation provided an opportunity to install a system of ORP sensors throughout the OBB. The OBB consists of (from bottom) coarse sand bedding underlying a CETCO Organoclay® Reactive Core Mat® (RCM), a GDL, a geotextile, and riprap for structural cover as shown in Figure 5. As tidal fluctuations flush oxygen and nutrients into the OBB via the geonet in the GDL, the OBB was expected to become more oxidized which would help facilitate oil degradation. These redox conditions were verified in real time by an IoT ORP monitoring system.

The objective of the field OBB monitoring study was to enhance our knowledge of OBBs and to demonstrate the value of installing IoT ORP sensors to monitor the redox conditions within an OBB. The field ORP data was expected to illustrate the effectiveness of the OBB in maintaining oxidizing conditions.

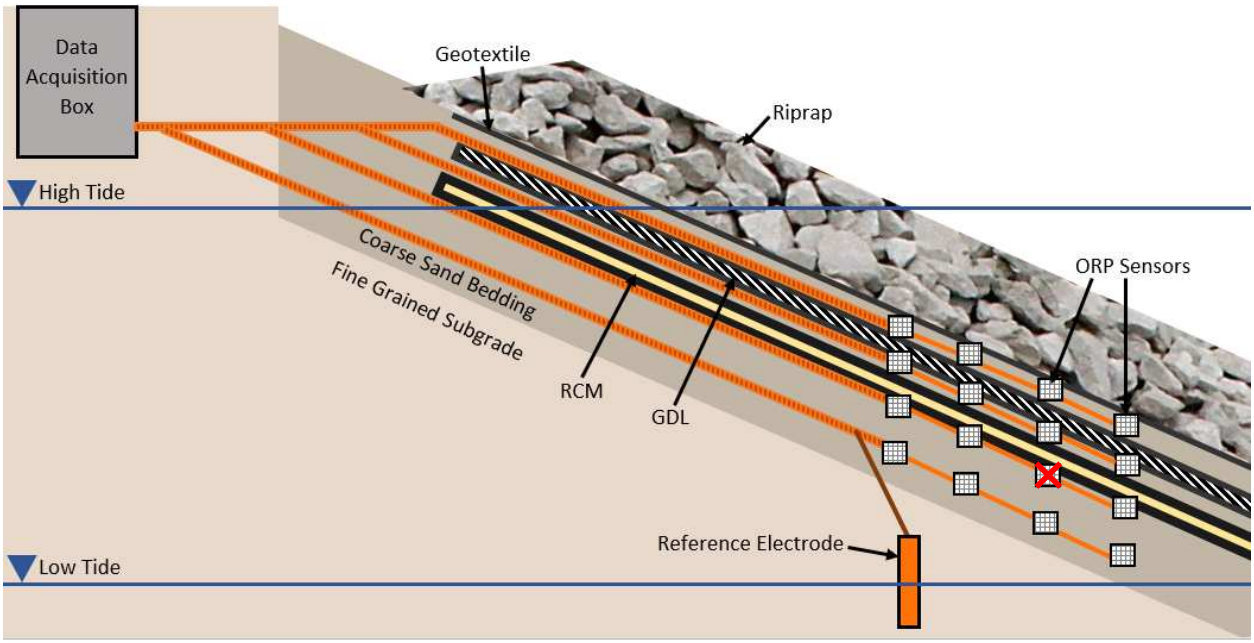

Figure 5. Field OBB and ORP sensor installation diagram.

3.2. Methods and Materials

Sixteen ORP sensing electrodes were made from titanium mesh cut into 25 mm by 25 mm squares. Five mm of ETFE wire coating was stripped off the end of a 22 AWG 1.37 mm wire (Alpha Wire, Elizabeth, NJ, USA), and the exposed portion of the wire was wrapped around a corner of the titanium mesh square. The corner of the titanium mesh square with the exposed wire was then fitted into a 3D printed epoxy housing and set in place with 3M ScotchWeld DP270 Clear 60-Minute Electric & Thermal Resistant Epoxy (3M, Saint Paul, MN, USA) as shown in Figure 6. Figure 7 shows the BORIN STELTH 1 Pd-$PdCl_2$ Reference Electrode (BORIN Manufacturing Inc., Culver City, CA, USA) that was used. This reference electrode was selected for long service life and resistance to fouling when exposed to oil.

Figure 6. Photo of a soil ORP sensing electrode with Sharpie marker for scale.

Figure 7. Photo of a BORIN STELTH 1 Palladium Reference Electrode

The field data logger used a Particle Electron processing board (Particle, San Francisco, CA, USA) to collect real time ORP data and upload data to the internet via 3G cellular service. The data logger circuit board is shown in Figure 8, and also included a

SparkFun 16 Channel Analog Multiplexer (SparkFun Electronics, Niwot, CO, USA) to accommodate 16 ORP sensors, an MCP3424 18-Bit ADC-4 Channel chip (Microchip Technology Inc., Chandler, AZ, USA) to convert analog signal to digital, and an Adafruit BME 280 pressure temperature and humidity sensor (Adafruit Industries, New York City, NY, USA) for temperature and humidity measurements within the datalogger box. The data logger was powered with 16 LG 3500 mAh 18650 batteries (LG Electronics, Seoul, South Korea). The data logger, batteries, and several silica gel desiccant packages were encased in an Ogrmar plastic waterproof IP65 junction box which was placed inside a Quazite PG concrete electrical enclosure (Hubbell Lenoir City, Inc., Lenoir City, TN, USA) at grade. Wires were run through slit corrugated sleeving conduit (McMaster-Carr, Elmhurst, IL, USA) and were passed through the bottom of the concrete electrical enclosure and threaded into the waterproof junction box through eBoot plastic waterproof adjustable cable gland joints. A Taoglas Roadmarker RG.02 4G cellular adhesive antenna (Taoglas, Minneapolis, MN, USA) was mounted onto the cover of the concrete electrical enclosure with JB-Weld waterproof marine epoxy (JB-Weld, Atlanta, GA, USA) as shown in Figure 9.

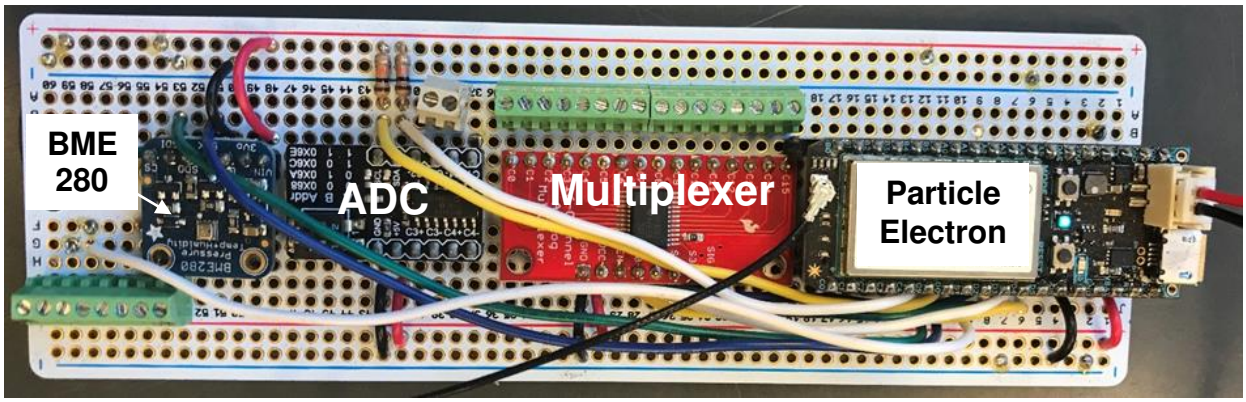

Figure 8. Photo of the field ORP data logger.

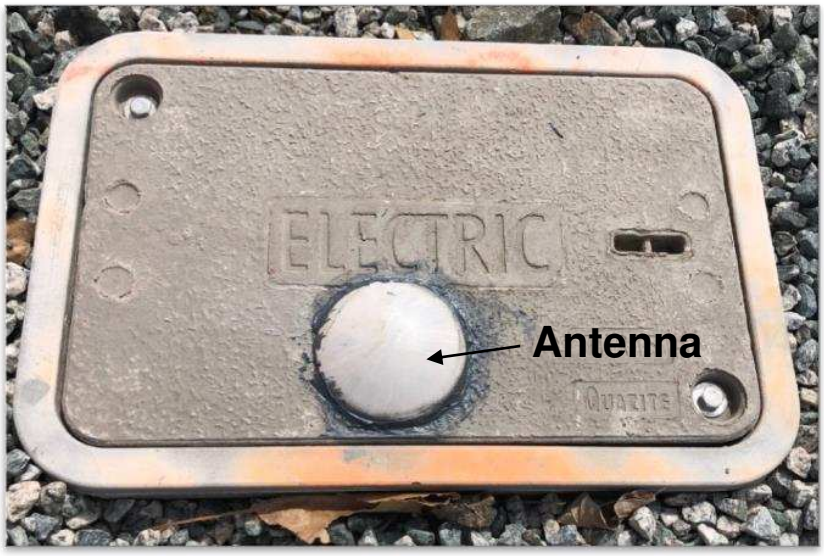

Figure 9. Photo of the cellular antenna mounted onto the concrete electrical enclosure.

The sixteen ORP sensors were divided into groups of four. Each group of sensors is herein referred to as a “string”. The four sensor stings are shown in protective conduits in Figure 10. A cofferdam was used to hold back the ocean while the OBB was installed.

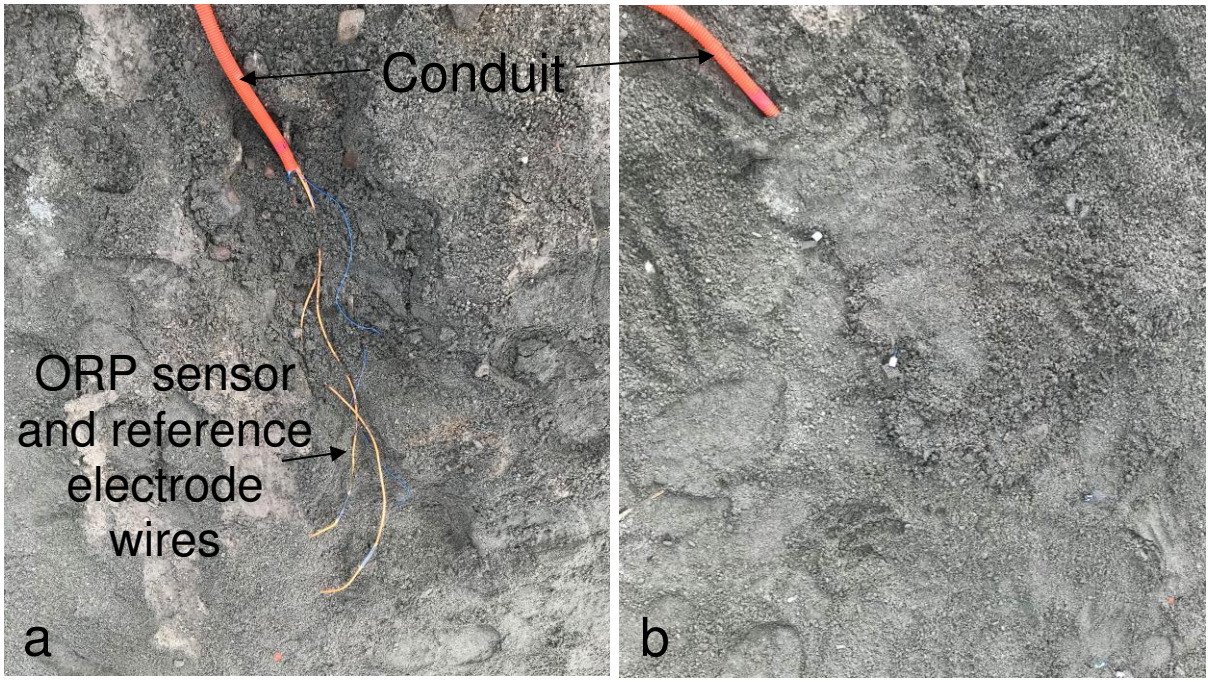

Figure 10. Photos of a) exposed and b) buried ORP sensors and reference electrodes in coarse sand bedding.

The OBB was installed between elevations of approximately -0.76 m to 1.5 m (NAVD 88). Water levels were expected to fluctuate between -0.75 m and 0.72 m (NAVD 88) and all sensors were installed between -0.10 m and 0.10 m (NAVD 88) to observe the effects of tidal fluctuation. Sensor strings were placed within different layers of the OBB during installation. The locations of the sensor strings and ORP sensors are shown in Figure 5. One sensor string (labeled “sediment” in the results section) with two reference electrodes was installed and buried in the coarse sand bedding as shown in Figure 10. The next sensor string (labeled “Below RCM” in the results section) was installed on the top of the coarse sand bedding just below the RCM as shown in Figure 11.

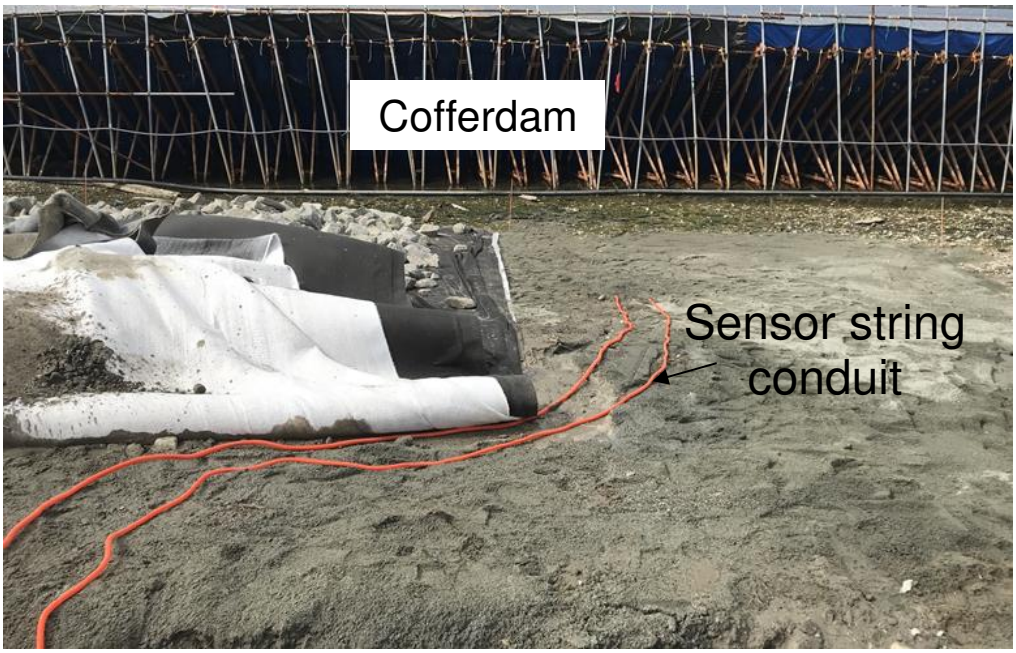

Figure 11. Photo of the sensor string installed on top of the coarse sand bedding.

Figure 12 shows the RCM layer being installed on top of the coarse sand bedding and Figure 13 shows the next string of sensors (labeled “below GDL” in the results section) installed on top of the RCM.

Figure 12. Photo of the RCM installation.

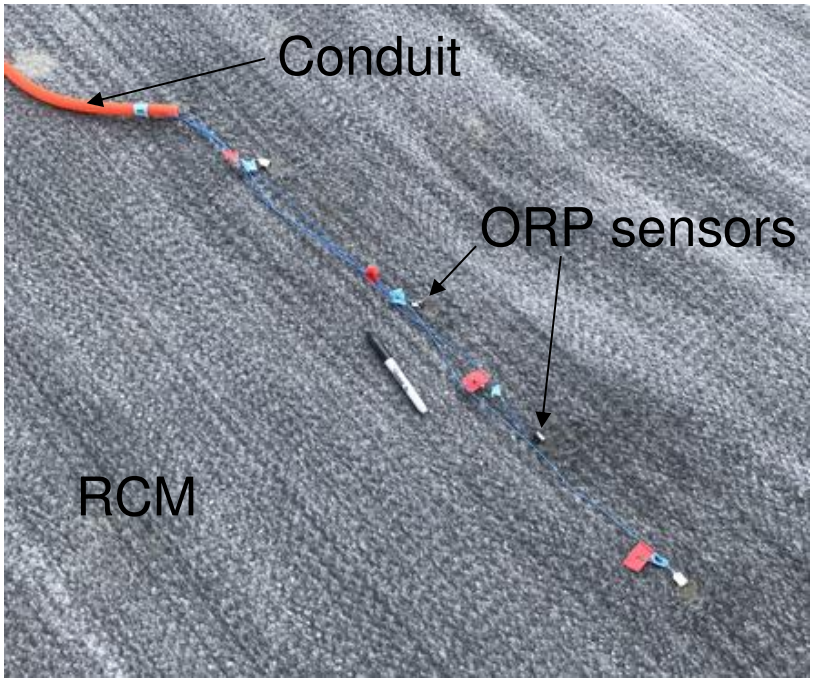

Figure 13. Photo of the sensor string installed on top of the RCM with a Sharpie marker for scale.

Figure 14 shows the GDL being installed and Figure 15 shows the final sensor string (labeled “above GDL” in the results section) being installed on top of the GDL.

Figure 16 shows the layers of the OBB installed in the anchor trench at the top of the GDL.

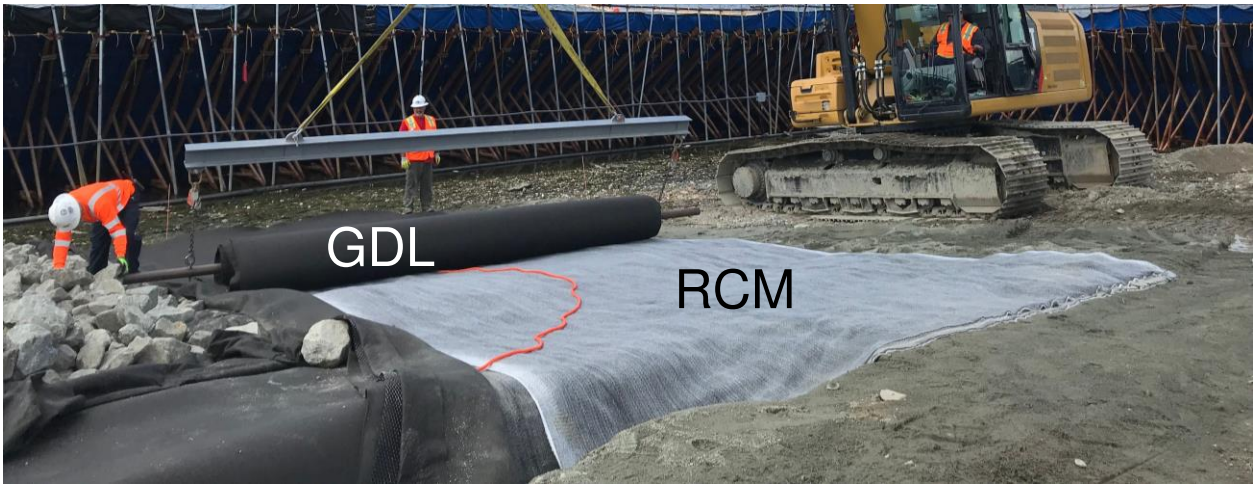

Figure 14. Photo of GDL installation.

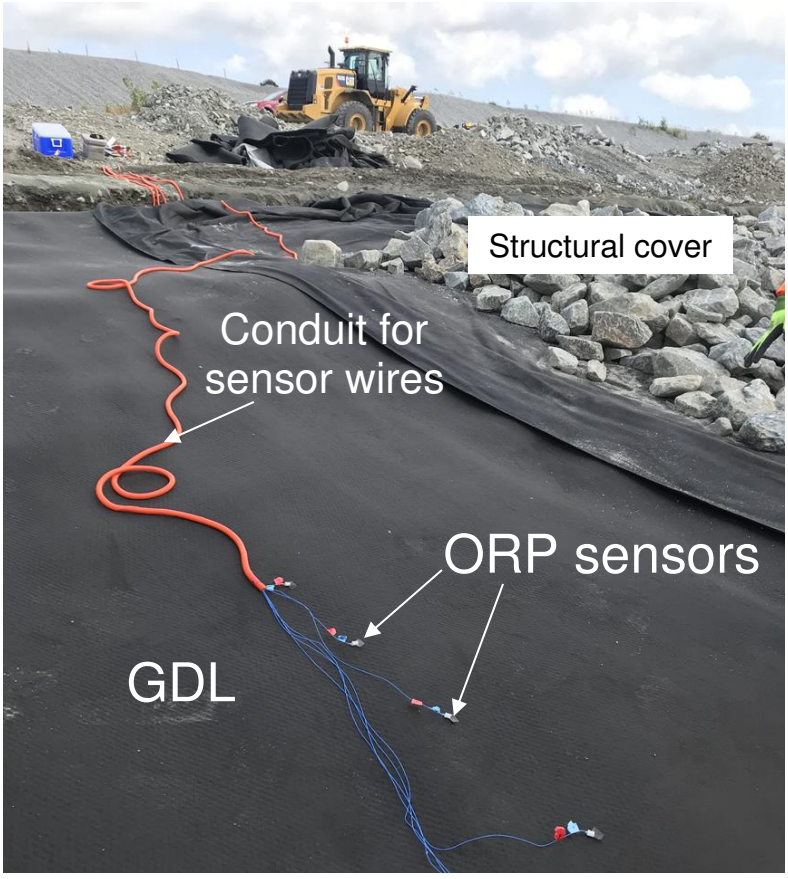

Figure 15. Photo of sensor string installed on top of GDL.

Figure 16. Photo of OBB anchor trench.

The foreground of the photo in Figure 17 shows a heavy geotextile that was installed on top of the GDL to protect the barrier layers from damage from the structural cover, and the background of picture shows the final structural riprap cover.

Figure 17. Photo of geotextile and structural cover layers of OBB.

Figure 18 shows the exposed and buried conduits leading to the upland data acquisition box and Figure 19 shows the site after the installation was completed.

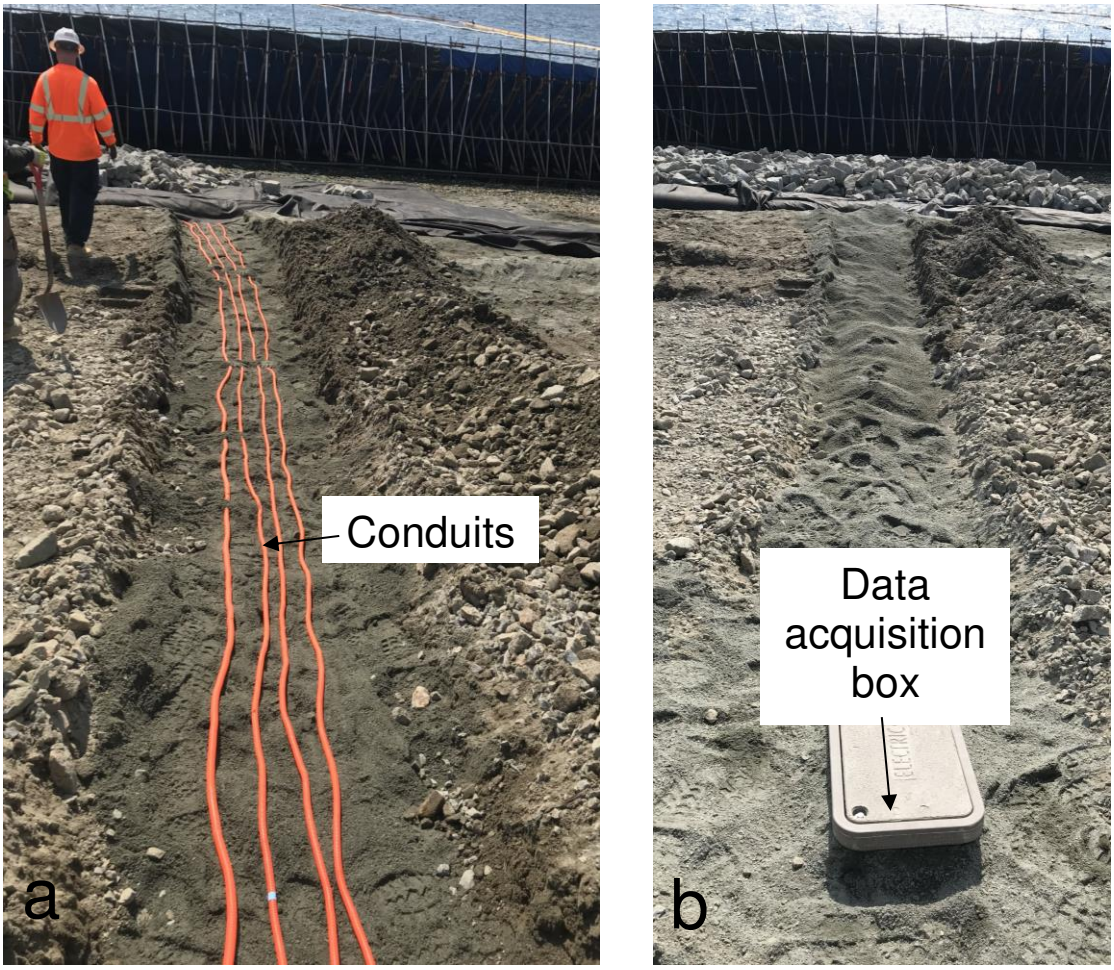

Figure 18. Photos of a) exposed and b) buried conduits leading to the data acquisition box.

Figure 19. Photo of the field site after OBB installation.

The required below grade completion of the data acquisition system created several problems including unreliable internet connectivity which led to infrequent collection of data points and decreased battery life. The Particle Electrons used to send data were originally set up to collect data at the top of each hour and were put into “deep sleep mode” for 55 minutes following data collection as a means of conserving battery. This strategy was counterproductive because the data loggers often took longer than the five minutes to connect to the internet after powering on which drained the battery faster than if the data loggers had been constantly powered on. The original monitoring system used two data loggers each powered by six batteries and is shown in Figure 20. These data loggers only collected data for 10 days before the batteries were completely drained.

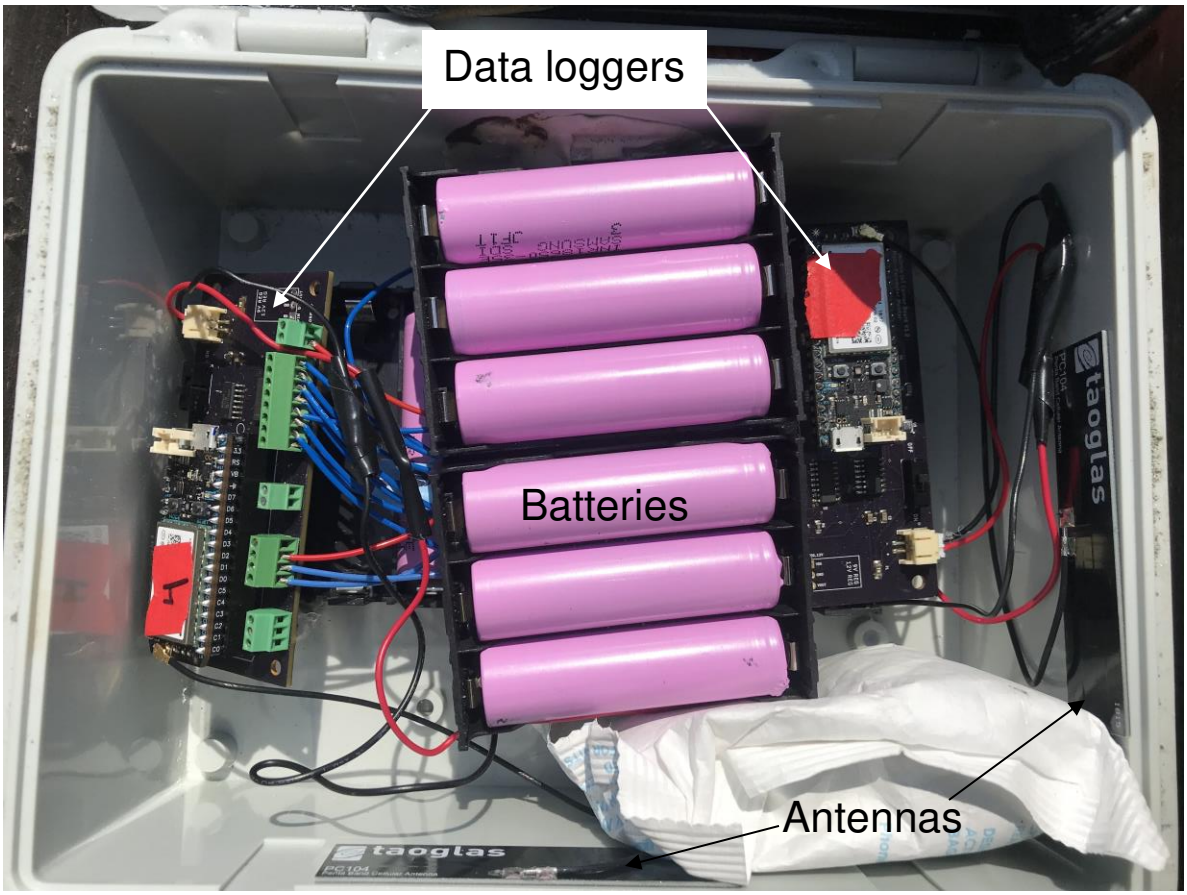

Figure 20. Photo of original field data loggers, antennas and batteries.

Internet connectivity issues were solved by designing and installing a new data logger described at the beginning of this section and shown in Figure 21. The antenna on the new data logger was mounted on the electrical vault lid to avoid any obstruction. Code for the electron processing board was updated to maximize battery life. Finally, the improved data logger was powered by 16 batteries instead of six. The improved data logger consistently collected ORP data every hour for over three months and was still collecting data every hour at the time this thesis was written.

The field OBB ORP data presented in this study was collected approximately six months after the OBB was installed, which provided time for microbial equilibration. Temperature and pH within the OBB and underlying soil were not measured, but ocean water pH is typically ~8.1 and the water temperature during the monitored period ranged from 41.3 °F to 45.3 °F (NOAA Station FOXR1).

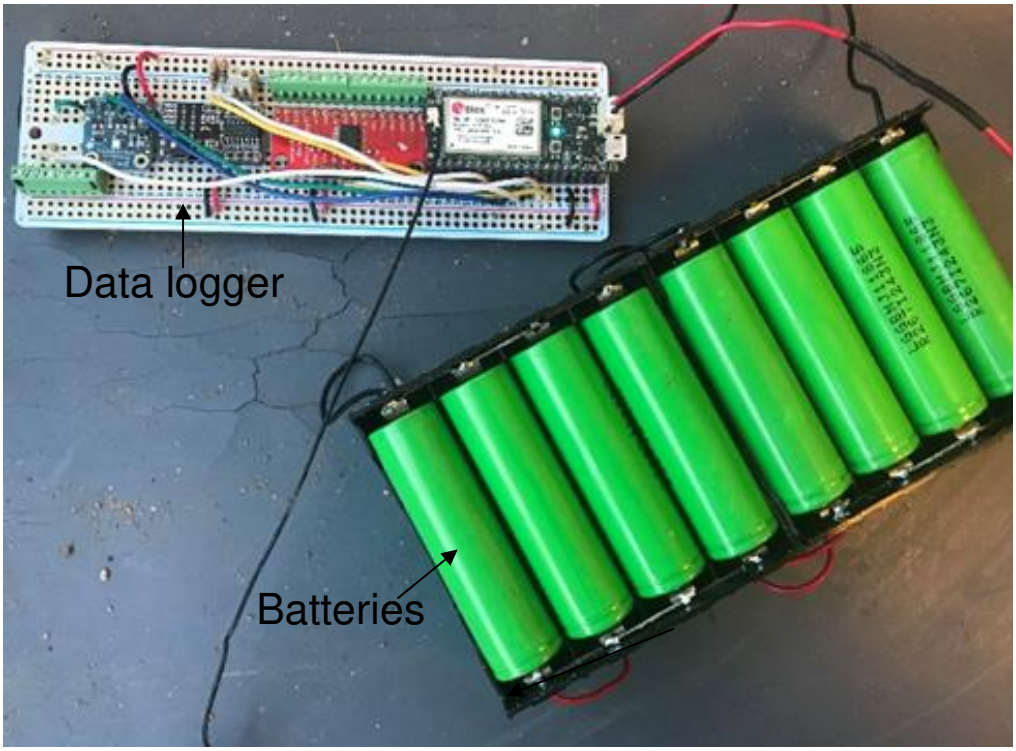

Figure 21. Improved field ORP data logger and batteries.

While these factors and several other physical, chemical, and biological conditions affected ORP within the cap, ORP values presented in the results were not corrected due to uncertainty of these factors in the OBB. In addition, within typical natural ranges these factors will not make an appreciable difference to the general results and conclusions of this study.

3.3. Results and Discussion

Fifteen of sixteen ORP sensors collected reliable data every hour for over three months. Spatial and temporal ORP data are displayed in GAS (Gallo, Askarani, Sale) plots in Figures 23, 24, and 25. The GAS plots labeled “Average” are based on the average ORP data from each sensor on one string depth, and the GAS plots labeled “A”, “B”, and “D”, are based on ORP data from single sensors on a specified stack as shown in Figure 22.

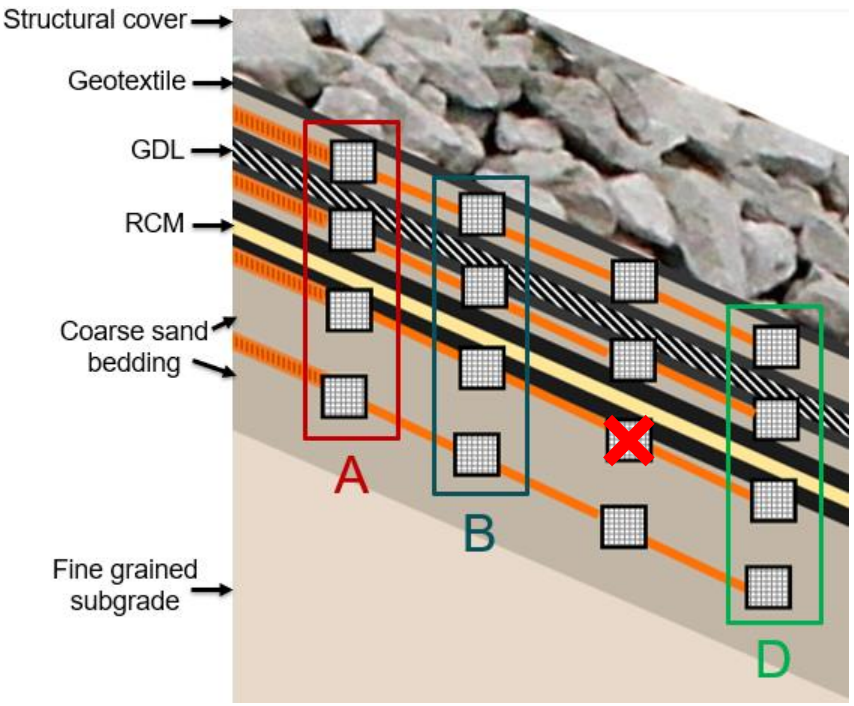

Figure 22. OBB sensor group diagram (red “X” indicates a failed sensor).

The GAS plots presented in Figure 23 illustrate how tidal fluctuations (US Harbors Station 8454000) over two days affect ORP in different layers of the OBB. Because there are two high tides and two low tides per day, a two day window was selected to show as much data as possible while also being able to discern trends as the OBB responded to flooded versus drained periods. This specific two day window was chosen because the time period was the longest from a preceding precipitation event in the available data, and precipitation events significantly affected the redox conditions in the OBB. The ORP values during this two day period remained between 385 mV to 525 mV (red and orange colors in the GAS plots). This range of ORP falls between the ORP values correlated with the oxygen and manganese redox couples. These data illustrate that redox conditions in the OBB stayed aerobic irrespective of tidal fluctuations.

The OBB did not experience significant changes in response to changing water levels. However, there are minor trends that align with tidal fluctuations that can help explain how the OBB functions. For example, as shown in Figure 23 there are slight surges in ORP of about 10 – 20 mV that indicate a shift towards the oxygen redox couple (orange parts of plot becoming darker orange or red) aligned with each rise and fall of sea level. This trend occurs for all levels, and perhaps is most apparent below the RCM. After each surge in ORP, redox conditions largely returned to their initial state. This trend may be due to the initial rush of oxygen from oxygenated surface water during flooded periods and the initial rush of atmospheric oxygen diffusing into the OBB during drained periods. This trend was most apparent on the interface between the OBB and RCM likely because the OBB enhanced drainage and oxygen delivery. The OBB also became more oxidized over time as ORP data from all sensors increased by about 10 – 20 mV from

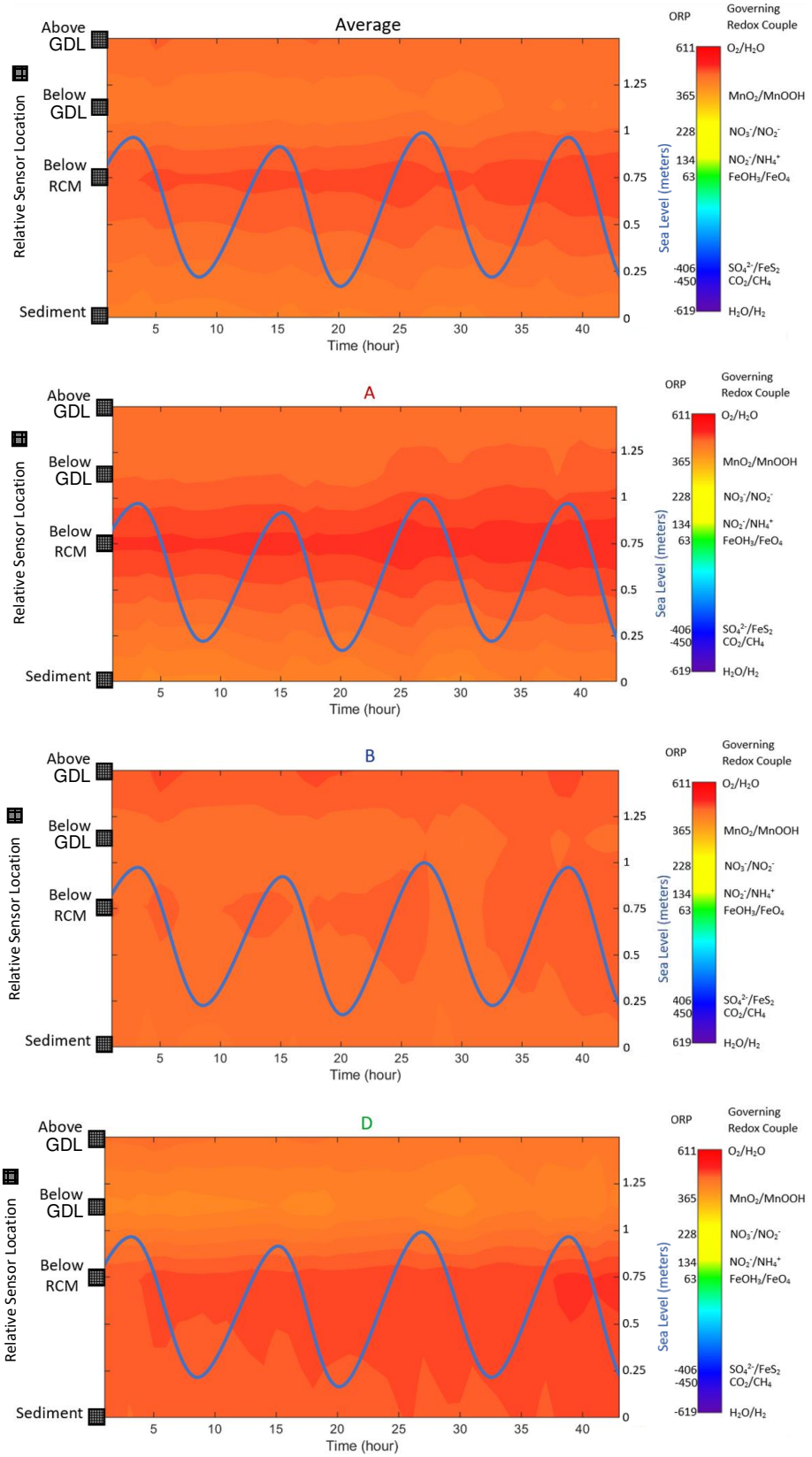

Figure 23. Field ORP GAS plots with tidal fluctuations over a two day period.

time 0 hours to time 48 hours which indicted a gradual shift towards the oxygen redox couple (lighter orange colors on the left side of the GAS plots and darker orange and red colors on the right side of the GAS plots).

The GAS plots in Figure 24 provide a comparison of the redox conditions in the OBB to precipitation events over a one month span shown in terms of cumulative rainfall. Immediately following rainfall events, the conditions in the OBB became more reduced, and ORP values approached the nitrate/nitrite redox couple. These abrupt drops in ORP following precipitation events ranged anywhere from 20 mV to over 300 mV and occurred over just a few hours (shown by colors in Figure 24 GAS plots changing from red-orange to yellow). In the following days, the OBB gradually became more oxidized until the next precipitation event occurred, and the cycle began again.

Redox conditions during the precipitation event located at about the 200 hour mark in the GAS plots in Figure 24 are shown in Figure 25. This specific precipitation event was the second most intense over the one month period displayed in Figure 24 and was selected because the precipitation event caused the most significant drop in ORP of all precipitation events throughout the month (up to a 320 mV drop). The redox conditions in the OBB exhibit a sharp decrease following rainfall (Figures 24 and 25), and in the hours immediately following the precipitation event, redox conditions quickly transition back to initial oxidizing states. The interface between the GDL and RCM (labeled “Below GDL”) is the most affected by precipitation (more reduced conditions indicated by the yellow parts of plot aligned with “Below GDL” sensor location). Additionally, precipitation events seems to affect redox conditions near the toe of the OBB more than any other area.

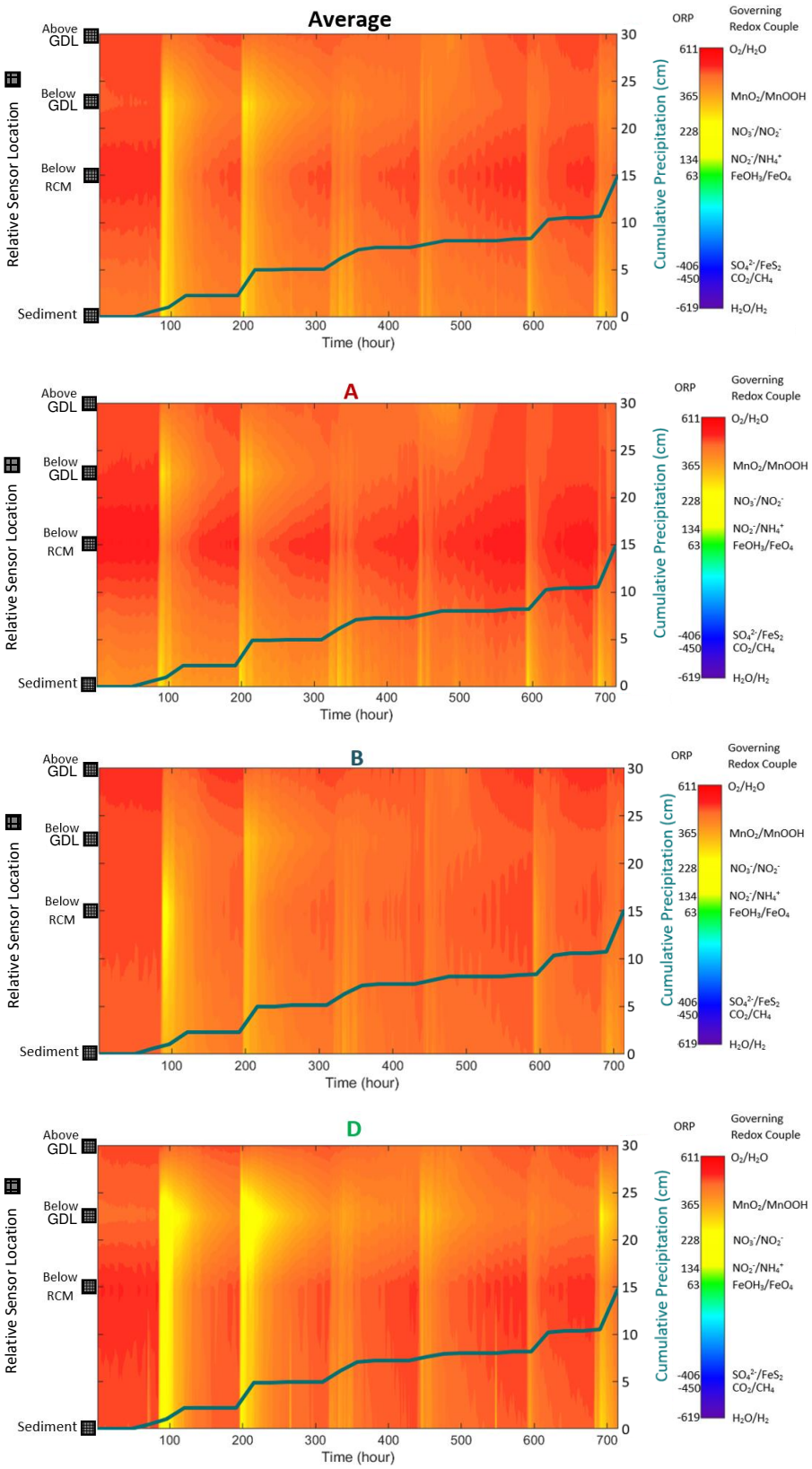

Figure 24. Field ORP GAS plots with cumulative precipitation over a one month period.

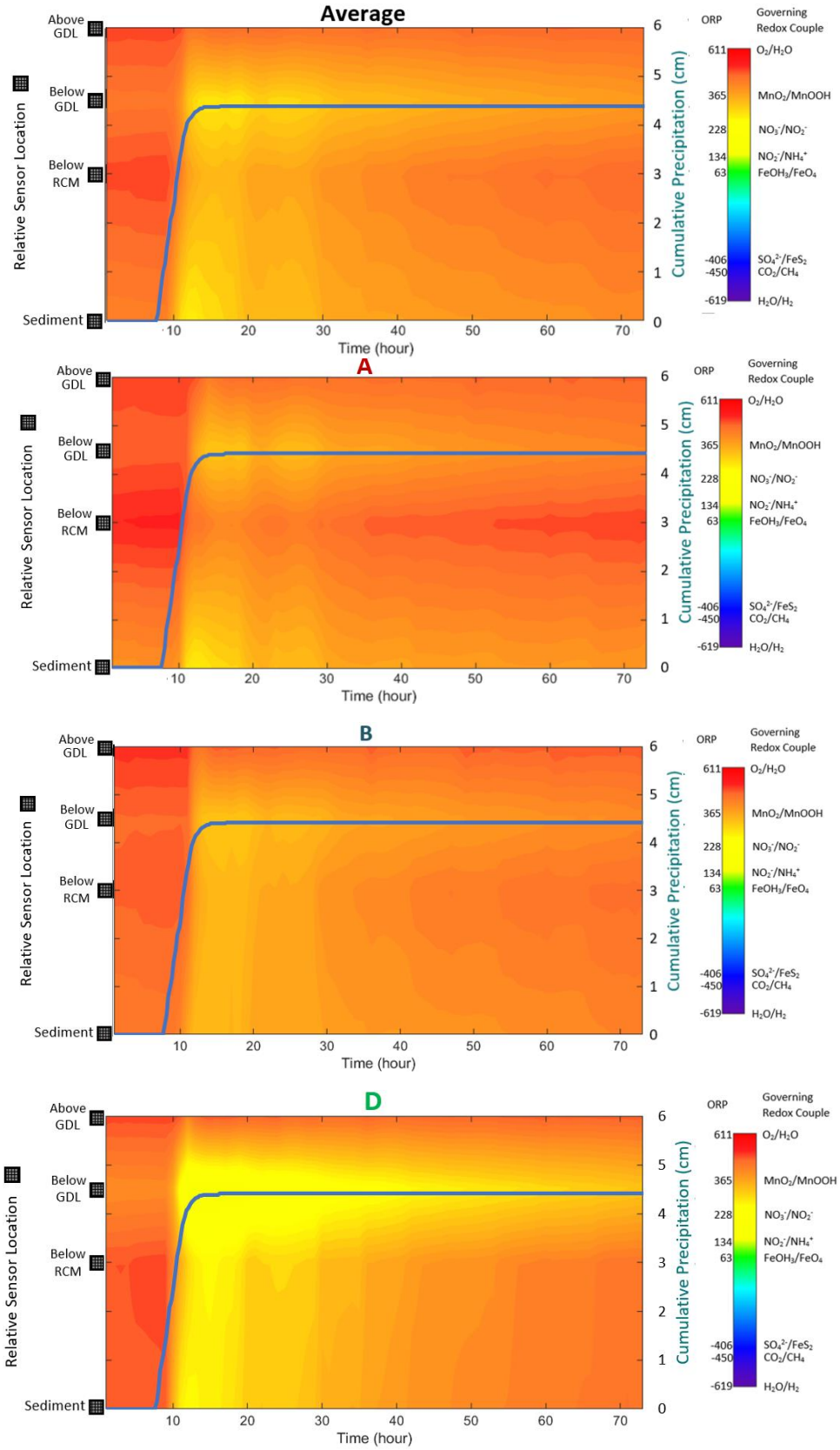

Figure 25. Field ORP GAS plots with cumulative precipitation over a three day period.

Interpretation of the GAS plots in Figure 25 are consistent with the observation that the OBB exhibited the most reduced conditions immediately following rainfall, and less reduced conditions in the following hours and days. This trend suggests reducing water flushed through the OBB in response to precipitation events. Since the fine grained subgrade is less transmissive relative to the protective cap, water is assumed to have drained within the OBB following precipitation. The most reduced conditions occurred in the layer between the GDL and RCM, which suggests the reducing water draining through the OBB preferentially flowed along this interface because of the high transmissivity of the GDL layer.

While the abrupt decreases in ORP in Figures 24 and 25 align with precipitation events, rainwater typically has an ORP between 200 – 320 mV (Goncharuk et al. 2010), so rainwater alone is unlikely reducing enough to cause this substantial drop in ORP. However, during construction, the anchor trench shown in Figure 26 was flooding with groundwater. Once the anchor trench was backfilled, upwelling groundwater and surface water runoff is hypothesized to have saturated the trench and became reducing due to the standing water limiting the inward diffusion of atmospheric oxygen. During precipitation events, rainwater would cause the reducing groundwater to overtop the anchor trench and travel downgradient through the cap, where the abrupt ORP drops were observed.

Similar to the lab OBB monitoring experiment, redox conditions directly above the OBB were more oxidizing than sensors below the OBB. This redox behavior may be due to water occupying the pore space of the bottom geotextile of the GDL. Due to gravitational forces, water draining through the OBB flows along the bottom geotextile,

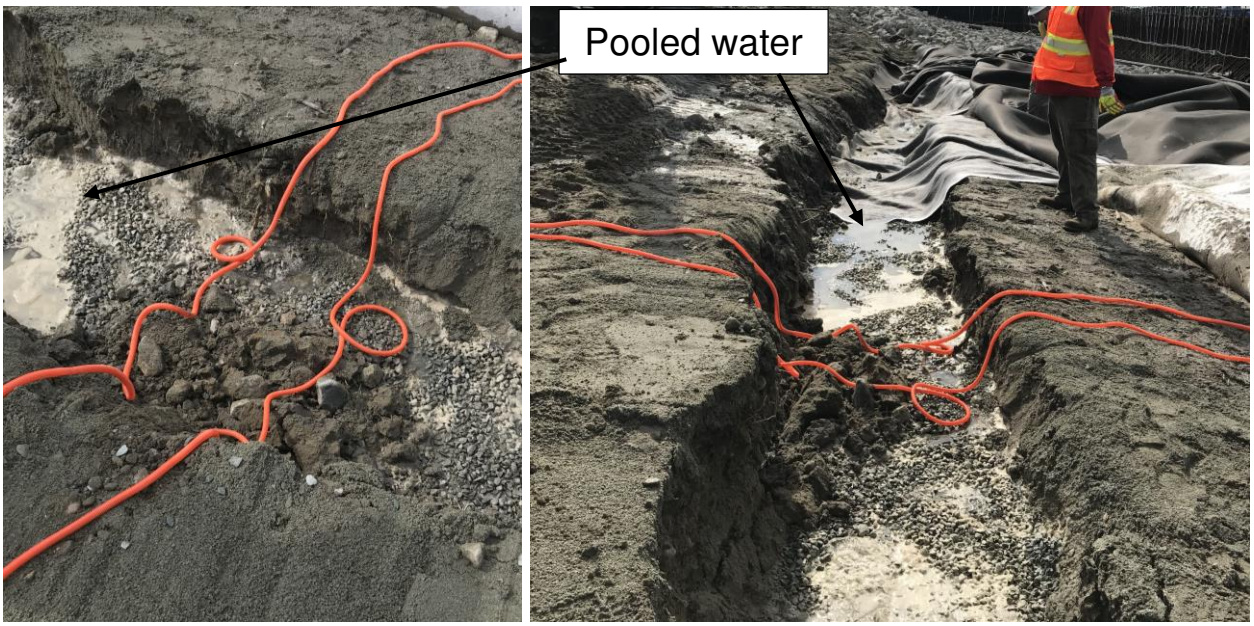

Figure 26. Photos of OBB anchor trench beginning to fill with groundwater.

causing the bottom geotextile to retain more water than the top geotextile during drained periods. This water retained on the geotextile may have limited oxygen diffusion into underlying sediments, causing ORP sensors beneath the GDL to exhibit slightly less oxidizing conditions. This behavior is different than the behavior that would be expected if the geotextile was saturated with oil. Completely degraded oil is oxidized to methane and carbon dioxide, and the methane/carbon dioxide redox couple is correlated with an ORP value of -450 mV against the Ag-AgCl or Pd-$PdCl_2$ reference electrodes. Therefore, an oil saturated geotextile would be expected to demonstrate more reduced redox conditions due to the presence of methane and carbon dioxide.

An OBB conceptual model hypothesized by Tochko (2018) incorporates redox cycling iron under an OBB as a basis for the absence of oil in the 10 cm layer of sediment directly beneath the GDL. Figure 27 illustrates how a bank of redox cycling iron can create

a barrier that rapidly degrades oil. Following Tochko (2018), oxidized ferric iron (Fe^{3+}) can act as a bank for redox reactions. As oil is introduced to this ferric iron species, a redox reaction occurs in which oil is used as an electron donor and ferric iron is used as an electron acceptor. The oil is then oxidized rapidly as ferric iron is reduced to a ferrous iron (Fe^{2+}) species. As oxygen diffuses into the OBB via the GDL, oxygen reacts with the ferrous iron species and is oxidized back into ferric iron and the redox cycle begins again. The Tochko (2018) OBB conceptual model is consistent with the ORP data collected in this study, verifying that the OBB is maintaining oxidizing conditions favorable for rapid aerobic degradation of oil.

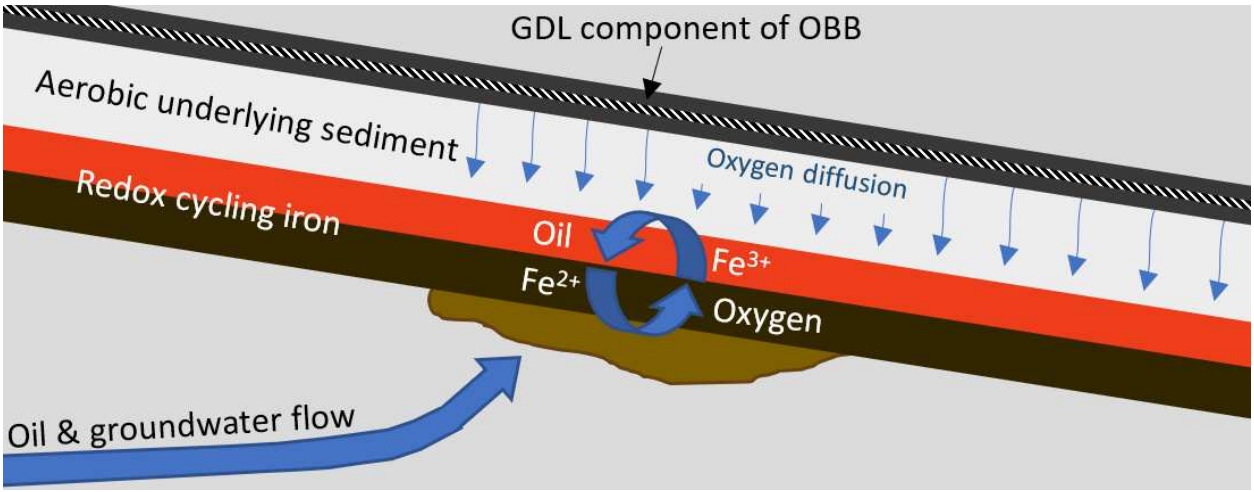

Figure 27. OBB with redox cycling iron diagram (after Tochko 2018).

Installing ORP sensors with IoT capabilities in an OBB supplies real time ORP data that is used to verify whether an OBB is effectively maintaining the oxidizing conditions necessary for the OBB to function as a sustainable oil-degrading bioreactor. Throughout the months of data collected, the ORP monitoring system confirmed that the redox conditions inside the OBB remained highly oxidizing. In the event of OBB fouling or sedimentation, the IoT ORP monitoring system could be setup to trigger an alert that

would indicate imminent OBB failure. These alerts could provide valuable time to act before oil overloads the OBB and forms a sheen.

4. LAB OLEOPHILIC BIO-BARRIER MONITORING

4.1. Experimental Objectives

The main objective of the OBB monitoring experiments were to determine if IoT ORP sensors could be a useful tool for monitoring OBBs. The ORP sensors differentiate aerobic and anaerobic zones, which help determine the extent of oxygen delivery and help further our understanding of the extent of the processes that govern the degradation of oil in an OBB. The specific objective of the laboratory sand tank experiment was to illustrate the effectiveness of the OBB in creating more oxidizing conditions in an environment that initially had highly reducing conditions and for which the water filling the OBB was reducing. A secondary objective of the laboratory OBB monitoring study was to test and troubleshoot the technology in a controlled environment before installing ORP sensors in the field.

4.2. Methods and Materials

The sand tank had dimensions of 91.4 cm by 30.5 cm by 40.6 cm with a 0.5 cm thick plexiglass sealed divider down the middle of the length that split the tank into two sections. A permeable metal screen was located 10.2 cm from one end of the tank as shown in Figure 28. For this experiment, only one half of the tank was used. Sediments used included gravel and coarse and fine Colorado silica sands. Additionally, a sand-bentonite barrier was formed using 250 cm^3 of fine sand, 250 cm^3 of Wyoming sodium bentonite, and 500 cm^3 of water. A non-woven geotextile was cut into four rectangles to fit the dimensions of the tank. The geotextiles were layered over gravel in the bottom of

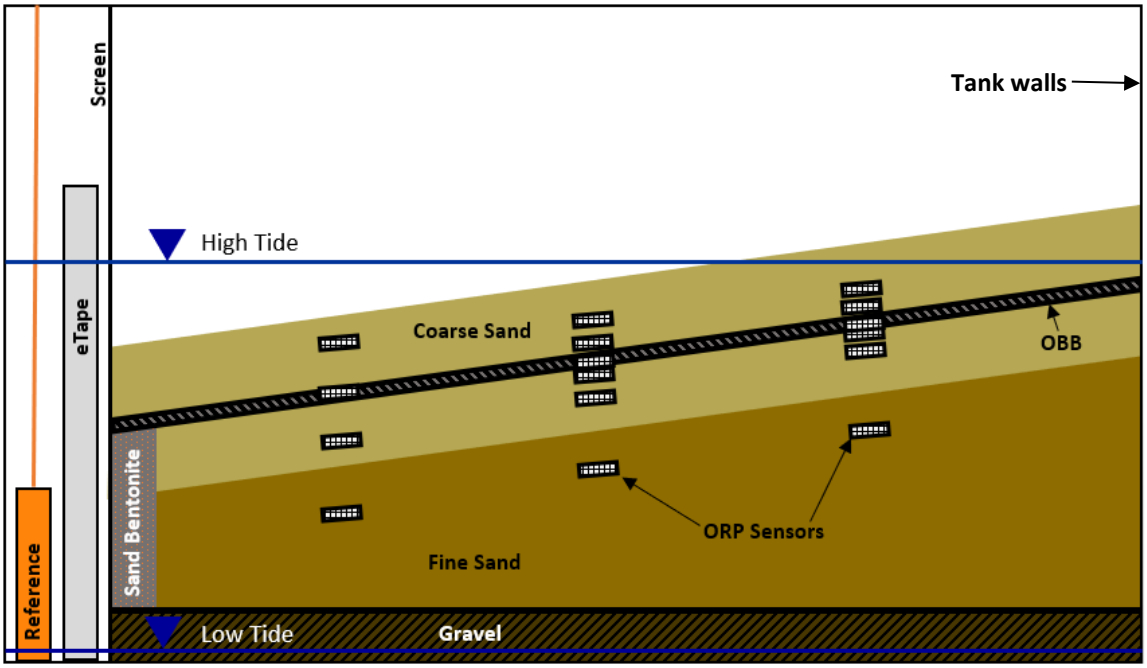

Figure 28. Sand tank OBB installation diagram.

the tank to serve as a drainage filter. A GDL was cut into a rectangle the width of the tank and 97 cm length and placed into the tank at an angle to allow for drainage. Momentive RTV 100 Series black silicone caulk (Momentive Performance Materials, Waterford, NY, USA) was used to seal the sides of the geotextile and OBB layers to the tank to prevent preferential flow around these layers.

The bottom of the sand tank was filled with gravel to a depth of 5 cm and covered with the four layers of geotextile to allow flow up through the bottom of the sediment. Sand bentonite paste was also used to seal the screen between the geotextile layers and the GDL as shown in Figure 28. Fine sand was placed at an angle of ~20° on top of the geotextile layer. A 7.6 cm thick coarse sand layer was placed on top of the fine sand. A GDL was placed above the coarse sand layer and caulk was applied between the two

long sides of the GDL. Another 7.6 cm thick coarse sand layer was placed on top of the GDL.

Sixteen ORP sensing electrodes were made from titanium mesh cut into 25 mm by 25 mm squares. Five mm of ETFE wire coating was stripped from the end of a 22 AWG 1.37 mm wire (Alpha Wire, Elizabeth, NJ, USA), and the exposed portion of the wire was wrapped around a corner of the titanium mesh square. The corner of the titanium mesh square with the exposed wire was then fitted into a 3D printed epoxy housing and set in place with 3M ScotchWeld DP270 Clear 60-Minute Electric & Thermal Resistant Epoxy (3M, Saint Paul, MN, USA). A BORIN STELTH 1 Pd-$PdCl_2$ Reference Electrode (BORIN Manufacturing Inc., Culver City, CA, USA) was used. This reference electrode was selected for a long service life and resistance to fouling when exposed to oil.

The lab data logger, as shown in Figure 29, used a Particle Photon processing board (Particle, San Francisco, CA, USA) to collect and transfer real time ORP data to the cloud via Wi-Fi. The processing board was mounted onto a printed circuit board designed by Zach Ferrie (Colorado State University). The lab data logger also included a SparkFun 16 Channel Analog Multiplexer (SparkFun Electronics, Niwot, CO, USA) to accommodate 16 ORP sensors and an MCP3424 18-Bit ADC-4 Channel chip (Microchip Technology Inc., Chandler, AZ, USA) to convert analog signal to digital.

Figure 28 shows where the ORP sensors were installed in the sand tank OBB. Three ORP sensors were installed within the GDL. Four sensors were installed in direct contact with the GDL (two above and two below). Six sensors were installed within the coarse sand surrounding the GDL, with sensors 2.5 cm above and below the GDL, 3.8 cm above and below the GDL, and 6.4 cm above and below the GDL to analyze the redox

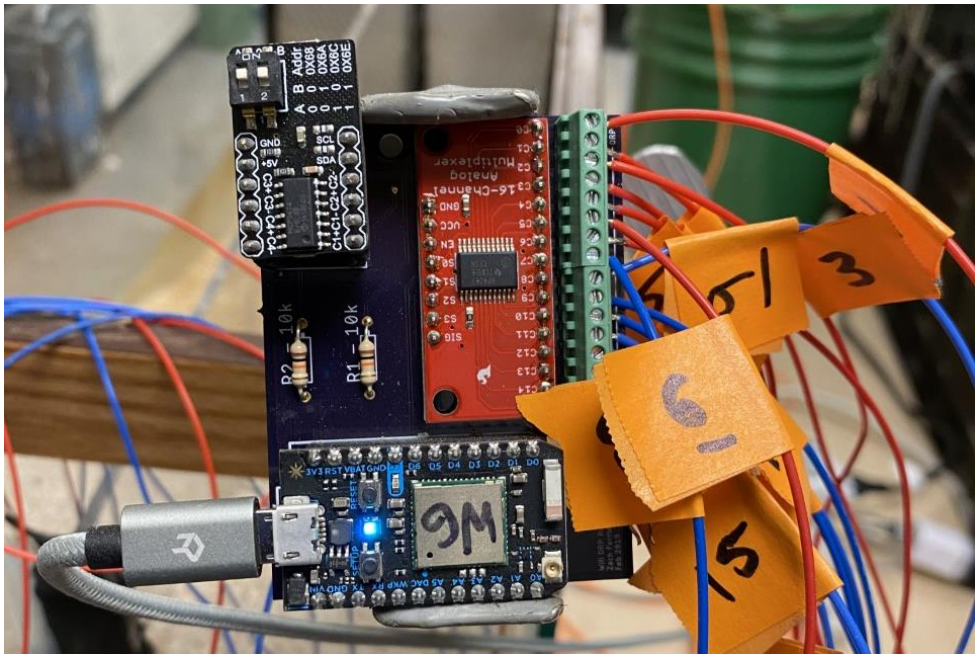

Figure 29. Photo of sand tank OBB ORP monitoring experiment data logger.

conditions at different distances from the GDL. The three remaining sensors were placed in the fine sand at depths of 2.5 cm, 5 cm, and 7.6 cm below the bottom of the coarse sand layer. The BORIN STELTH Pd-$PdCl_2$ Reference Electrode was placed in the sand tank on the empty side of the screen, and can be seen on the left in Figures 28 and 31. A 31 cm eTape Liquid Level Sensor (Milone Technologies, Sewell, NJ, USA) was used in conjunction with a Particle Photon processing board (Particle, San Francisco, CA, USA), as shown in Figure 30, to monitor water level in the sand tank in real time.

Water collected from College Lake (Fort Collins, CO, USA) on November 19, 2019 was mixed with molasses to a concentration of 5 µg/L and was pumped into the tank to a depth of 30.4 cm. The carbon rich molasses with microbially active lake water were left to sit for four weeks. After two weeks the sand tank achieved highly reducing conditions indicative of methanogenesis (ORP < -450 mV) and is shown in Figure 32. These

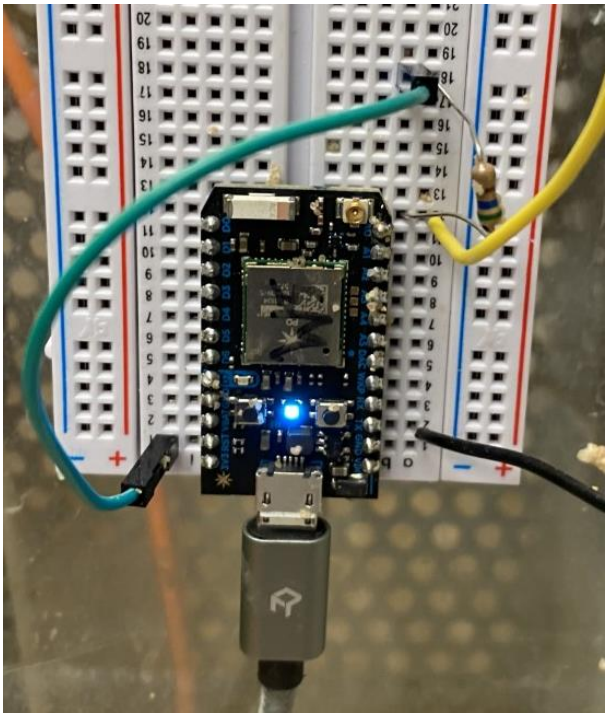

Figure 30. Photo of eTape data logger.

Figure 31. Photo of as-built sand tank OBB.

conditions were meant to simulate a worst case scenario in which an OBB was installed in a highly reducing environment and was flushed with reducing water. By installing an OBB in this environment, the goal was to assess if the GDL could still effectively shift the redox poise throughout the OBB even under unfavorable conditions.

Figure 32. Photo of the OBB sand tank after achieving highly reducing conditions.

After equilibrating to a methanogenic redox couple, daily drain/fill cycles began where the sand tank was then drained for 12 hours and filled for the next 12 hours at a rate of ~70 mL/hour every day for about four weeks to simulate tidal conditions. The pumps used for the drain/fill cycles were Ismatec REGLO model peristaltic pump with Ismatec 3-Stop Chem-Durance® Bio 2.79 mm ID pump tubing (Cole-Parmer, Wertheim,

Germany) and Tygon ND-100-65 Class V1 medical delivery tubing (Saint-Gobain, Courbevoie, France).

4.3. Results and Discussion

In the sand tank OBB experiment, ORP responded significantly to changing water levels. Before beginning the daily tidal fluctuations, the highly reducing ORP values in the sand tank were correlated with the methanic redox couple (< -450 mV). Once daily drain/fill cycles were initiated and ORP fluctuations became regular, only the deepest depths of the fine sand achieved ORP values indicative of the methanic conditions. The rest of the OBB either remained within the ORP range correlated with the iron redox couple or shifted between ORP values correlated with the sulfidic and iron redox couples in response to changing water levels. Figure 33 shows the conditions in the sand tank OBB after two weeks of water level fluctuations where the changes in ORP became regular and most sediments in the sand tank OBB returned to a light brown color except for a strip of reduced black fine sand about 8 cm thick in the bottom of the tank. The water in the sand tank had a neutral pH and the tank was in a room temperature lab, so correcting ORP for pH and temperature was not considered necessary.

Figure 34 labels each sensor, shows the relative positions of these sensors within the OBB, and divides the OBB into three sensor levels labeled “lower”, “middle”, and “upper”. Figure 35 shows three ORP GAS plots. GAS plots present ORP data spatially (y-axis) and temporally (x-axis) with ORP assigned a color based on a spectrum from -619 mV to 611 mV consistent with the redox ladder shown in Figure 3 in Chapter 2. Data from 9 of 16 ORP sensors were interpreted to indicate shifts between redox couples in

response to daily drain/fill cycles. The color key to the right of each gas plot correlates specific colors to common redox couples and corresponding ORP values. Shifts between redox couples are indicated by changing colors in Figure 35, where warmer colors represent more oxidized conditions and cooler colors represent more reduced conditions.

Figure 33. Photo of the sand tank OBB after two weeks of daily drain/fill cycles.

The axes labeled “Elevation (cm)” in Figure 35 begin at the topmost sensor and end at the lowermost sensor. GAS plots depicting redox conditions in the lower level of the OBB (Figure 35a) show more reduced conditions than redox conditions in the middle level of the OBB (Figure 35b) and redox conditions in the middle level (Figure 35b) of the OBB remain within the range of the iron redox couple (green color) longer than in the lower level (Figure 35a). Likewise, the middle level of the OBB shows more reduced conditions than the upper level, as Figure 35c shows more indication of iron and nitrogen redox

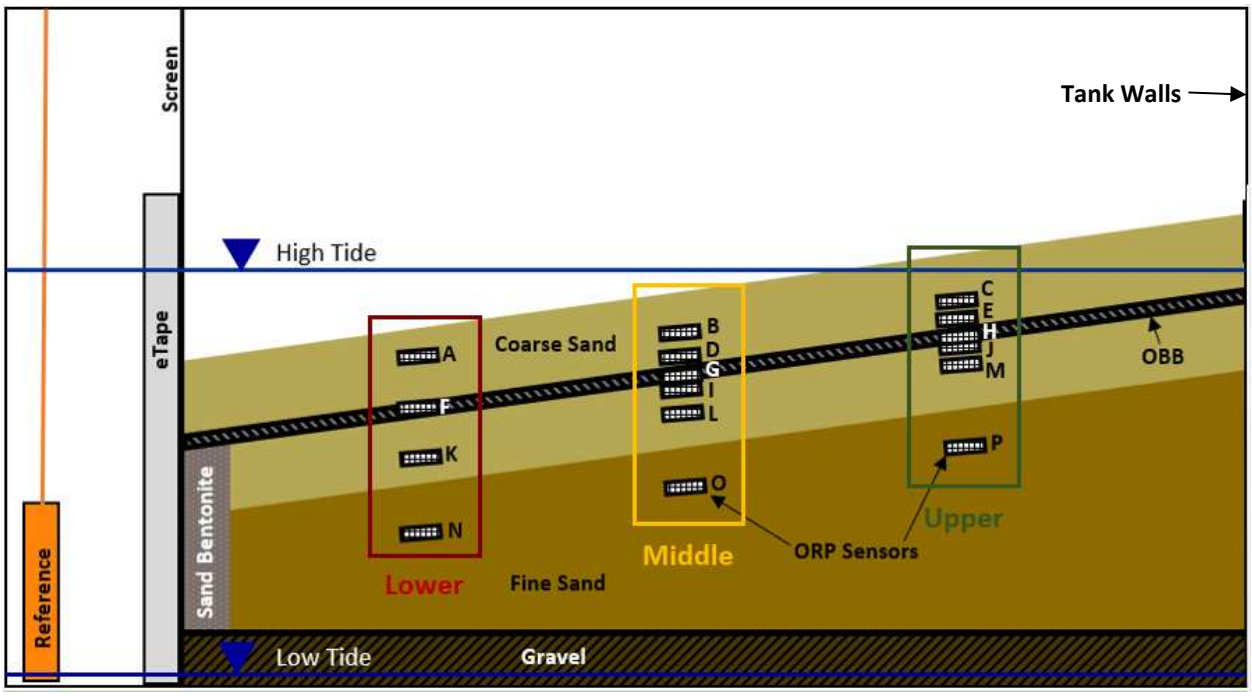

Figure 34. OBB sand tank diagram with sensor locations and levels.

couples (warm green and yellow colors) throughout the plot than Figure 35b. Therefore, oxygen delivery is interpreted to be reduced to parts of the system that are flooded for longer periods of time. In contrast, the lower level (Figure 35a) shows the presence of iron reducers (green color) penetrating further into the sediment than in the middle level (Figure 35b). However, the two lowest sensors on each level are spread about 10 cm apart, so the ORP in the soil between these sensors is uncertain.

The bottommost sensors are in the fine sand (labeled N, O and P) in Figures 34 and 35. Sensors N and O demonstrate highly reduced conditions indicative of methanogenesis during flooded periods and shift to sulfidic conditions during drained periods. In contrast, sensor P demonstrates a shift between the sulfidic and iron redox couples in response to changing water levels. This difference in redox conditions throughout the fine sand is further illustrated in Figure 33 where sensor P is located in the light brown fine sand and

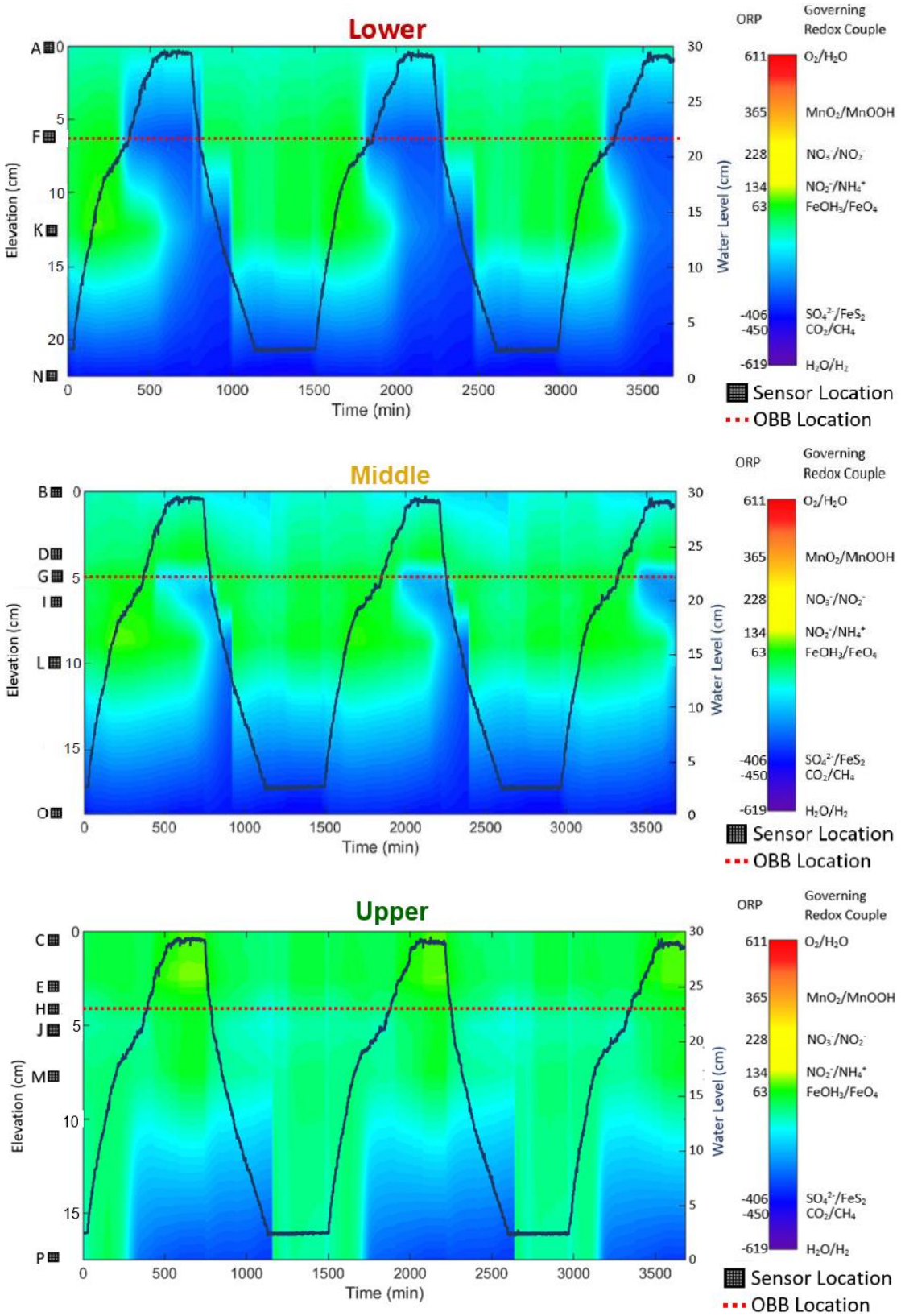

Figure 35. ORP GAS plots of the a) lower, b) middle, and c) upper levels of the sand tank OBB.

sensors N and O are located in the black fine sand which had a strong sulfur odor upon deconstruction of the sand tank. Although the data shows the water level dropping below the fine sand, the fine sand layer likely retained water during drained periods due to capillary forces. By constantly retaining water, the oxygen diffusion into the fine sand was limited, and likely caused the highly reducing redox conditions in the sediment, sulfur odor, and dark black color.

Although redox conditions mostly correlated to how long a section of the OBB was submerged, interpretation of ORP data suggests that the OBB was effective in creating a more oxidizing environment through oxygen delivery via the geonet in the GDL. As an example, displayed in the middle (Figure 35b) and upper (Figure 35c) level OBB GAS plots, sensors D and E are located directly above the GDL and show more positive ORP values than the sensors located just below grade (Sensors B and C) despite being submerged for longer, which illustrates the ability of the GDL to deliver oxygen to surrounding sediments. Similarly, the redox potential within the GDL is more oxidized than the redox potential of the uppermost sensors for the lower and upper levels of the OBB (Figures 35a and 35c) and is about the same for the middle level (Figure 35b). However, the middle and upper level GAS plots (Figures 35b and 35c) show that the redox conditions inside the GDL or directly beneath the GDL consistently exhibit lower ORP values than the sensors on top of the GDL. This trend is mirrored in the field OBB monitoring data and is further discussed in Chapter 3.

Although the sand tank OBB is interpreted to have created a more oxidized environment, more research is necessary to confirm this conclusion. The next step for this experiment is to recreate the sand tank OBB setup with a failed (silted-up) GDL and

compare redox conditions to assess if the GDL is the critical component of this system. This experiment was set up, but not completed due to COVID-19 lab shutdowns in the spring of 2020 limiting laboratory access; next steps are described in Appendix A, Section A.1.2.

5. RETENTION CAPACITY OF CANDIDATE OLEOPHILIC MATERIALS

5.1. Introduction

The geotextile component of the OBB is critical to preventing oil sheens by "catching" upwelling oil but allowing passage of gasses. The retention capacity of the oleophilic geotextile governs the maximum allowable oil loading an OBB can handle in the absence of biodegradation, and sites that experience higher loading may require a more robust oil retention system than a typical OBB. In this chapter, the geotextile component of the GDL is assessed to quantify oil retention capacity. Five oleophilic materials were tested including thin black (232 g/m^2), medium black (380 g/m^2), thick black (1055 g/m^2), and thin white (244 g/m^2) geotextiles, as well as woven coconut fiber (cocofiber) which was rolled into 1-cm-thick braids to simulate the woven components of a coir mat.

5.2. Experimental Objectives

A series of sorption experiments were conducted on candidate geotextile components of an OBB. The objective of these sorption experiments was to understand and quantify the sorptive capacity of different oleophilic materials for use within OBBs (neglecting oil degradation).

5.3. Background

Non-woven geotextile oil sorption capacity experiments have been performed in two previous studies targeted at OBBs (Chalfant 2015; Tochko 2018). Both studies tested the retention capacity of a GDL with "typical" geotextile components, which are herein

referred to as “medium black” geotextiles. Chalfant (2015) performed three experiments to determine the GDL retention capacity. The first was a “dip test” in which a rectangular GDL sample of known mass was submerged in diesel for 20 minutes. The GDL was then removed from the diesel and held horizontally to allow any excess diesel to drain, and the final mass was measured and recorded. The second GDL retention experiment performed by Chalfant (2015) was a “disk test” in which a GDL disk of known mass was submerged into diesel for 20 minutes. The GDL disk was then held horizontally and attached at the mid-point to an electric drill. The drill was turned to the highest speed for 10 seconds to allow the GDL to drain, and the final mass of the GDL was measured. The final GDL oil retention experiment performed by Chalfant (2015) was a “column test” in which a GDL disk was cut to fit the inside of a 10.16 diameter PVC column. The GDL was suspended in the middle of a water filled column and sealed in place with o-ring gaskets to eliminate flow along the edges of the column. Diesel was pumped into the bottom of the column at oil loading rates of either 0.06, 0.2, or 1 mL/min. When sheens were observed on the water surface, the time to sheening and the total volume of diesel pumped into the column at the point of breakthrough were recorded. Based on the results of these three oil retention capacity experiments, Chalfant (2015) concluded that the GDL with medium black oleophilic geotextile components retained 3 L of oil (diesel) per m^2. Tochko (2018) performed an OBB sand tank experiment in which a GDL was installed between layers of sand and the sand tank was flooded with de-aired water. Diesel was then pumped into the bottom of the sand tank over 76 hours where diesel was able to float up to and load the GDL. Tochko (2018) estimated the amount of diesel pumped into the tank at the point of breakthrough to be ~250 mL, which translated to an apparent oil

retention capacity of 3 L/m^2. However, this retention capacity was likely overestimated because some portion of the diesel pumped into the tank remained in the sand underneath the GDL.

5.4. Methods and Materials

Two experiments (dip test and diesel bubbling test) were performed in this study to determine the oil retention capacities of five oleophilic materials for potential use in an OBB. The apparatus used for the diesel bubbling test included a 40.6 cm length of 2.38 mm ID Tygon ND 100-65 Medical Tubing (Saint-Gobain, Courbevoie, France) which was fixed to the inside of a 1000 mL Pyrex glass beaker (Pyrex, Charleroi, PA, USA) using Momentive RTV 100 Series black silicone caulk (Momentive Performance Materials, Waterford, NY, USA). The length of tube was run down the side of the beaker with one end of the tube positioned at the midpoint of the bottom of the beaker and the other end connected to a 60 mL syringe filled with diesel. Two additional lengths of the 2.38 mm ID tubing were fixed to the sides of the beaker with one end of the tubes positioned halfway down the side of the beaker and the other end of the tubes connected to two 100 mL syringes used to fluctuate the water level. A final 0.8 mm ID tube was run down the side of the beaker with one end of the tube positioned at the midpoint of the bottom of the beaker directly across from the diesel injection tube, and the other end connected to a 10 mL syringe filled with air. Oleophilic materials were cut to fit the 10.2 cm inner diameter of the beaker. The edges of the material were fixed to the inside of the beaker with black silicone caulk to prevent flow around the boundaries. The beaker was then filled with water above the geotextile, but shallow enough for the water fluctuation syringes to drain

the water in the beaker to a level below the oleophilic material. A conceptual diagram of the experimental setup is shown in Figure 36.

Candidate oleophilic materials included thin black (232 g/m^2), medium black (380 g/m^2), thick black (1055 g/m^2), and thin white (244 g/m^2) geotextiles as well as one-cm thick cocofiber braids. The dip test was performed a minimum of three times and up to eight times (to evaluate test repeatability) for each candidate material. For the diesel bubbling test, the cocofiber was not tested and the medium black geotextile only underwent one trial while the thin black, thick black, and thin white geotextiles underwent four to six trials each.

For the dip test, candidate oleophilic materials of known mass and area were submerged in either diesel or crude oil for a minimum of one minute. Soaking materials for longer was determined to yield negligible changes in retained mass. The saturated materials then were suspended vertically so that excess oil could drain from the sample. The oleophilic materials were placed under varying compressive stresses during testing ranging from 7 kPa to 48 kPa to evaluate the effect of overburden stress. However, compression over this range of stresses did not affect the retention capacity of the materials. Finally, the oil saturated materials were weighed to determine the total mass of oil retained.

For the diesel bubbling test, oleophilic materials were suspended in water and loaded with diesel. The test was performed under a UV light to observe the fluorescence of the diesel to more easily detect diesel sheens due to breakthrough. When the oleophilic material was overloaded and a sheen formed on the water surface, the final volume of diesel was recorded at the time of breakthrough to determine the maximum volume of

diesel that could be retained before failure. The geotextile was then removed and photographed under UV light to determine the approximate diesel wetted area.

Retention capacity data are presented in a mass of oil per mass of oleophilic material basis as well as a volume of oil per area of oleophilic candidate material basis. The cocofiber retention capacity was only considered on a mass per mass basis because the area of the cocofiber braids could not be readily determined in a manner comparable to the nonwoven geotextiles. Similar to experiments performed by Chalfant (2015) and Tochko (2018), GDLs were tested, but the addition of the geonet component of the geocomposite did not affect the retention capacity of the materials, so the geotextile components of the GDLs were removed and tested separately; results presented do not include the complete geocomposite retention capacities (these are summarized in Table A5 in Appendix B).

5.5. Results and Discussion

The diesel bubbling test conceptual diagram shown in Figure 36 illustrates how diesel was pumped into the beaker. The “diesel blobs” shown in Figures 36 and 37 show how diesel would act as a non-wetting fluid with water as the wetting fluid. The “diesel/air bubbles” shown in Figure 36 show how diesel acted as an intermediate wetting fluid between water (wetting fluid) and air (non-wetting fluid). As these bubbles were carried through the oleophilic material via buoyant forces, the oleophilic material stripped the diesel off the bubbles as the air was able to pass through to the water surface. The diesel blobs accumulated underneath the thin black and thin white oleophilic materials instead of spontaneously imbibing across the material after 1 – 2 mL of diesel was injected into

the beaker. This is hypothesized to be due to water wetting the geotextile's polymer surface due to capillary forces. Then, as diesel blobs with water as the wetting fluid and diesel as the non-wetting fluid moved upwards in the beaker and came into contact with the geotextile, they were unable to spontaneously imbibe across the geotextile due to water occupying the geotextile's pore space. The water saturated geotextile caused the water-wet diesel blobs to settle on the underside of the geotextile. When these diesel blobs formed, water levels in the beaker were dropped to drain water from the oleophilic candidate material, and then raised again where the diesel was able to more easily imbibe across the oleophilic material. Water level fluctuations were also intended to simulate the tidal conditions that an OBB would experience at a GSI. As the water level dropped below

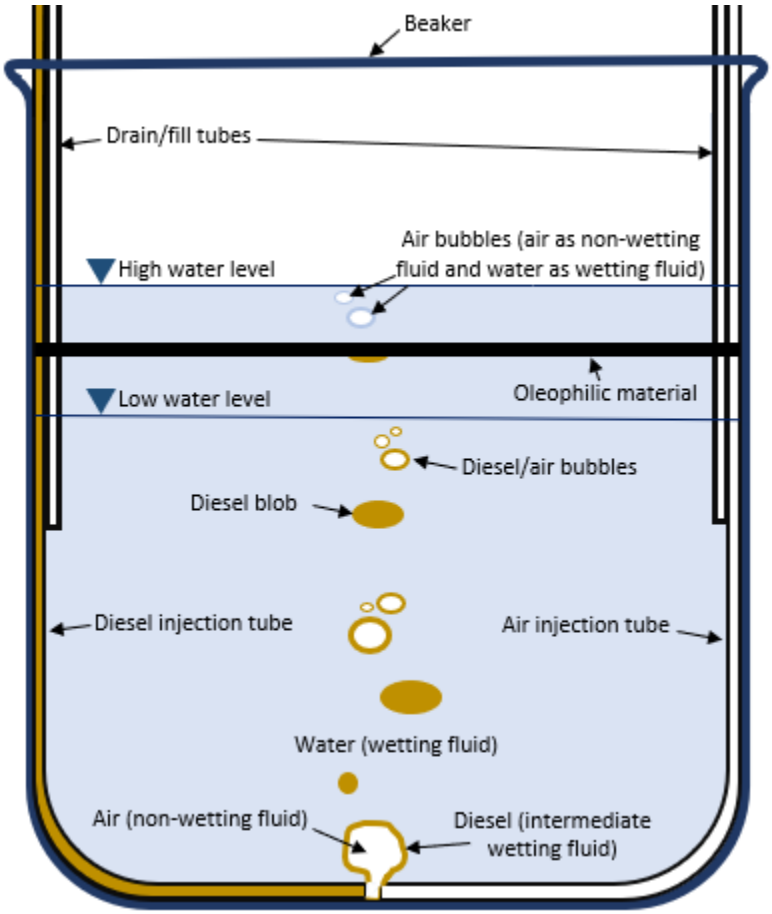

Figure 36. Diesel bubbling test beaker diagram.

the geotextile, the diesel blobs spread out across the water surface where the diesel became the intermediate wetting fluid, and the air became the non-wetting fluid. Then, by restoring the water levels, the diesel was able to more easily imbibe across the geotextile.

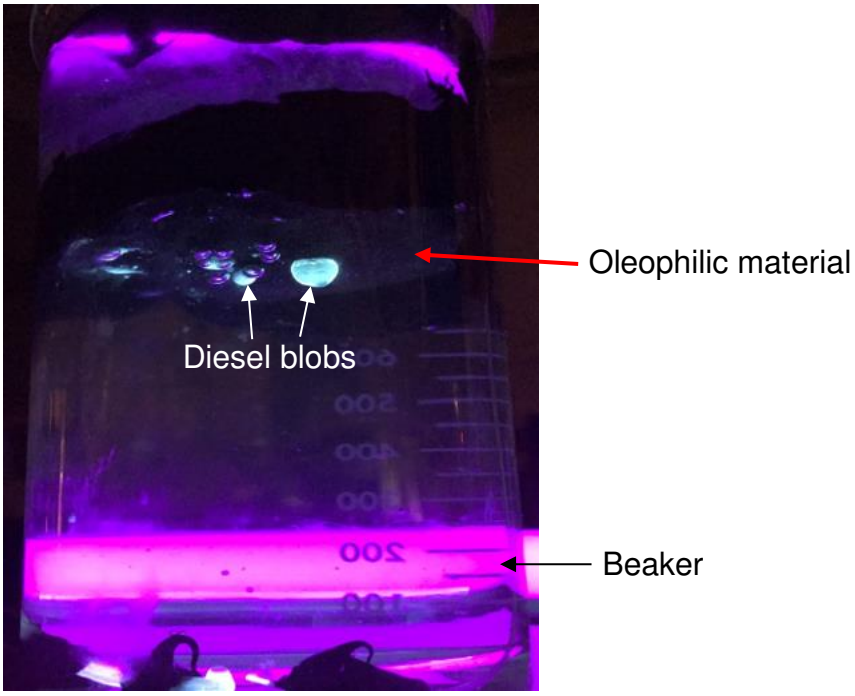

Figure 37. Photo of diesel blob formation during diesel bubbling test.

Figures 38 and 39 show the diesel and crude oil retention of the geotextiles and cocofiber tested. As shown in Figure 38, the thin white geotextile retained the most diesel (9.8 g/g) and crude oil (13.7 g/g) on a per mass basis, while Figure 39 shows that the thick black geotextile was able to retain the most diesel (7.4 L/m^2) and crude oil (8.1 L/m^2) on a per area basis.

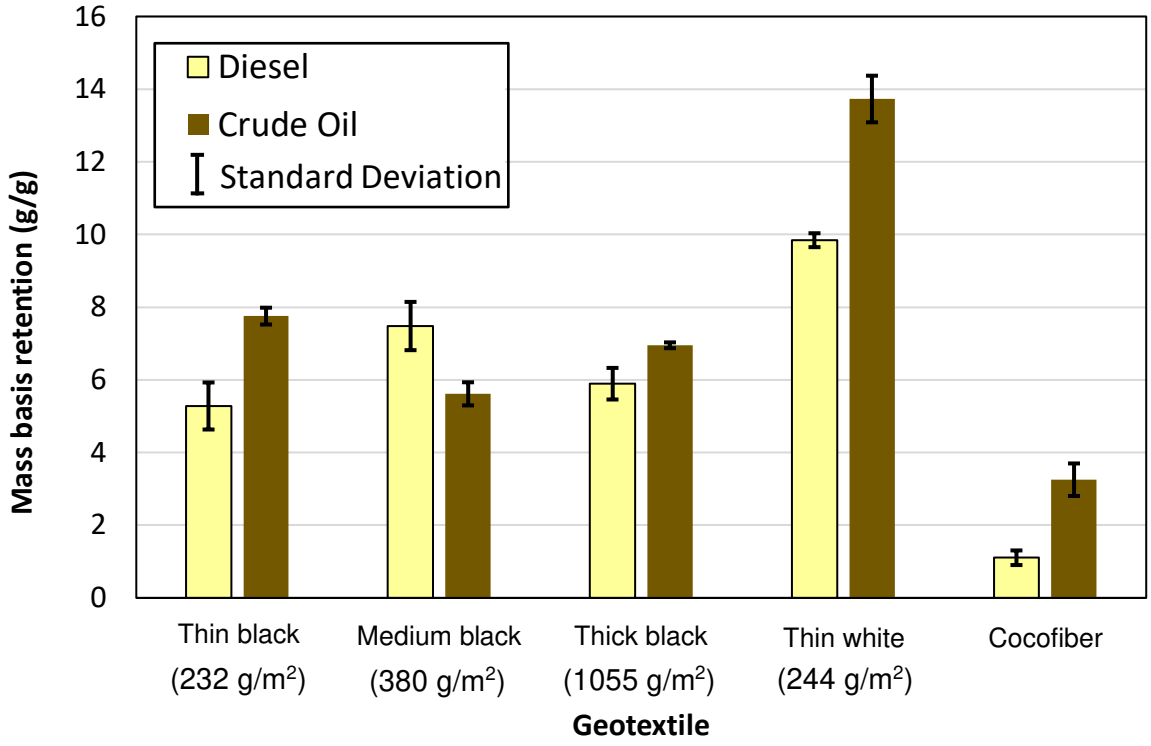

Figure 38. Comparison of oleophilic material retention capacities by dip test for diesel and crude oil on a mass-per-mass basis.

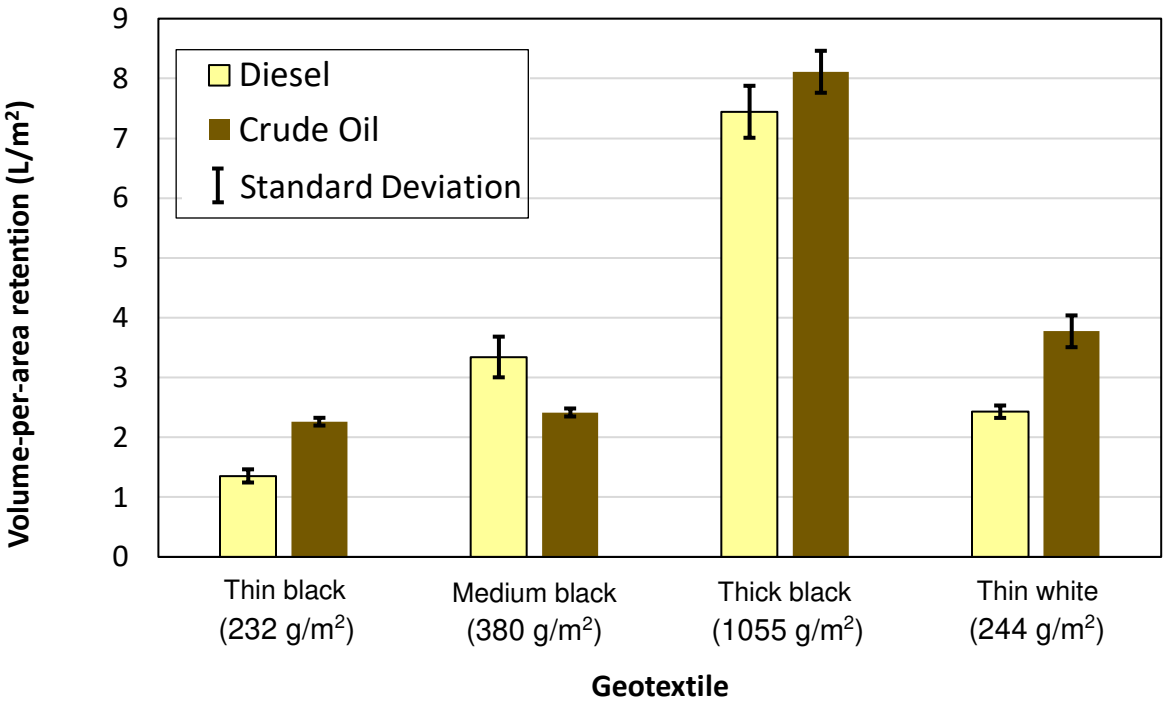

Figure 39. Comparison of oleophilic material retention capacities by dip test for diesel and crude oil on a volume-per-area basis.

The results from the diesel bubbling test illustrate that the thick black geotextile provided the most protection against breakthrough. The average retention capacity of the thick black geotextile at the point of breakthrough on a volume per area basis was 3.6 L/m^2 which was substantially greater than the retention capacities of the thin black, medium black, and thin white geotextiles (0.3, 1.1, and 0.6 L/m^2, respectively). Figures 40 and 41 show these retention capacities compared to retention capacities determined by the dip test. The medium black geotextile only underwent one trial, so results do not include standard deviation.

Figure 40 shows that the volume-per-area retention capacities of diesel determined from the dip test were at least four-times greater than the retention capacities

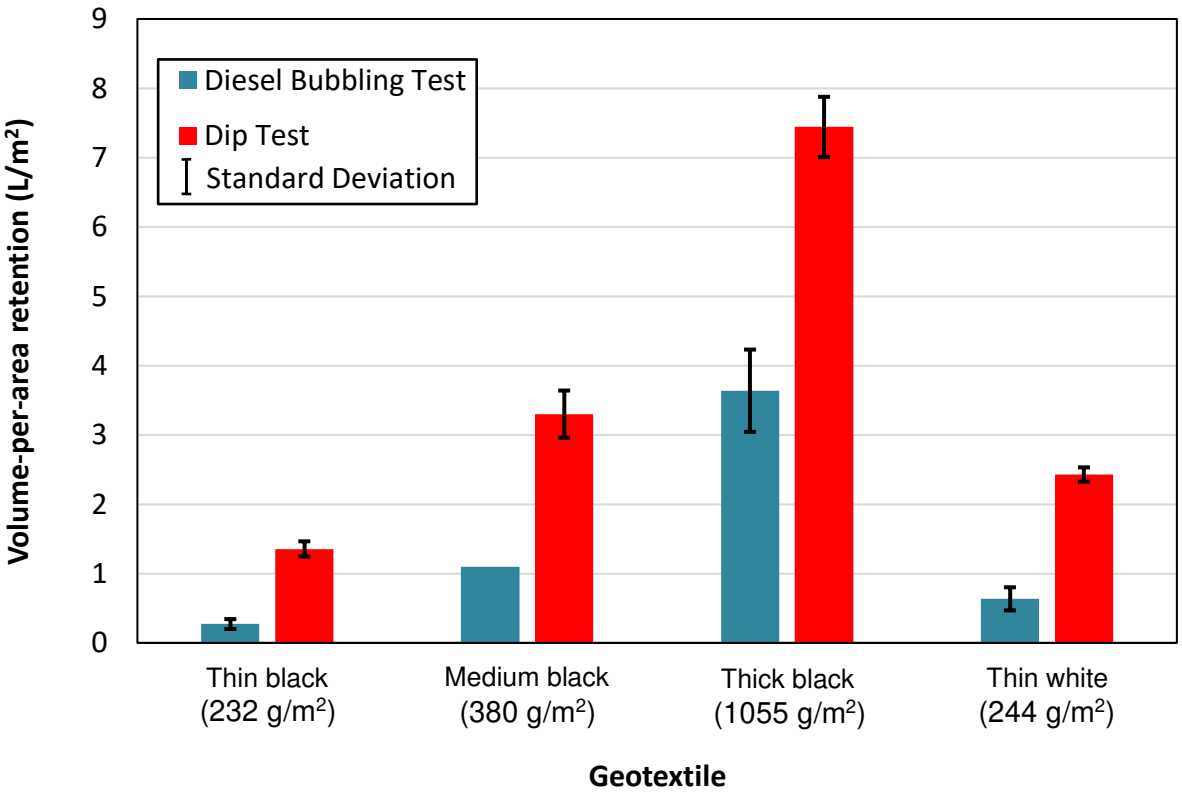

Figure 40. Bar graph comparing oleophilic material volume-per-area retention capacity in dip test and diesel bubbling test.

determined from the diesel bubbling test for the thin black and thin white geotextiles. The medium black and thick black geotextiles diesel retention capacities determined from the dip test were triple and double that determined from the diesel bubbling test, respectively. Similarly, Figure 41 shows that the mass-per-mass retention capacities determined from the dip test were at least double and up to more than five-times greater than the retention capacities determined from the diesel bubbling test, where the largest differences are again seen in the thin black and thin white geotextiles. This lower retention capacity by the diesel bubbling test relative to the dip test is likely due to the introduction of preferential flow paths in the diesel bubbling test, which loaded the geotextiles unevenly, and caused diesel to overload the geotextiles more quickly.

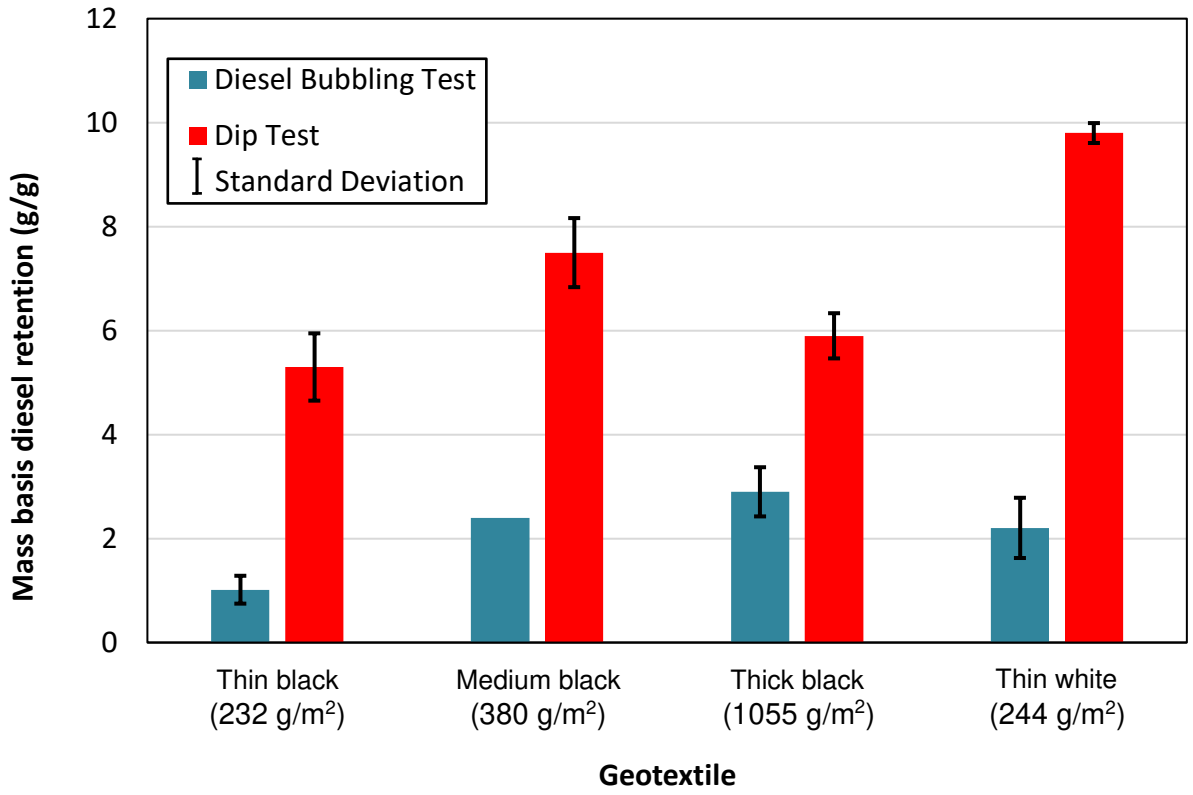

Figure 41. Bar graph comparing oleophilic material mass-per-mass retention capacity in dip test and diesel bubbling test.

Results from Chalfant (2015) showed the opposite relationship between the retention capacities determined in the dip test and column test (diesel bubbling test). Chalfant (2015) determined that the typical OBB geocomposite retained 3.25 L/m^2 of geotextile in the column test compared to 3.1 L/m^2 in the dip test. The conflicting relationships could be due to the difference in diesel loading rates, as slower loading rates may have allowed the diesel to displace water in the geotextile pore space and more thoroughly imbibe across the area of the geocomposite. Despite the similar experimental procedures, the diesel bubbling tests showed that the medium geotextile retained about 2/3 of what was retained in the column experiment from Chalfant (2015).

Results of both geotextile retention experiments show that the thick black geotextile retained more diesel and crude oil than the other candidate oleophilic materials on a per area basis. The thick black geotextile also retained the most diesel on a per mass basis in the diesel bubbling test. Therefore, the thick black geotextile is expected to provide the most robust protection against breakthrough when considering a single geotextile. However, based on results from the dip test, multiple layers of thin white geotextile may provide a greater overall retention capacity. Additional research is needed to identify other material properties that may control the performance of these materials in the field.

The mechanism hypothesized for why the thick black geotextile provided the most protection against breakthrough in the diesel bubbling test was because oil spontaneously imbibed across a greater area than was observed for the other geotextiles. Oil spreading across a greater area of the geotextile reduces the likelihood for a preferential flow path to overload one hotspot of the OBB, thus delaying the time to breakthrough. Figure 42

shows examples of each geotextile photographed under a UV light after breakthrough. The approximate percentage of each geotextile that was wetted by diesel was ~33% for the medium black geotextile and ranged from 20% to 33% for the thin black geotextile, 75% to 90% for the thick black geotextile, and 25% to 50% for the thin white geotextile.

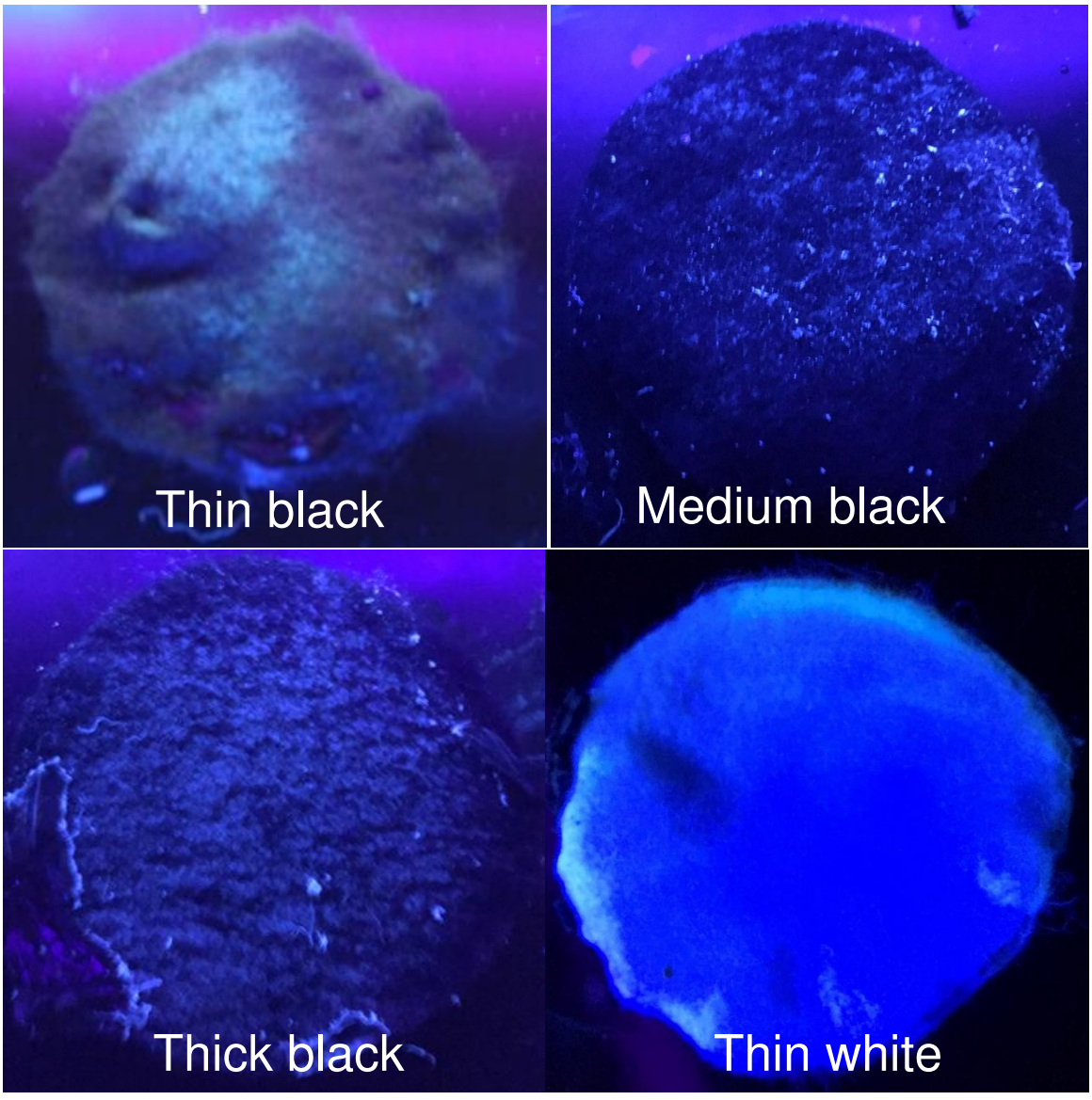

Figure 42. Photos of oleophilic materials under UV light after being removed from the diesel bubbling test beaker.

The medium black, thin black, and thin white geotextiles retained less diesel and crude oil than the thick black geotextile on a per area basis. However, the retention capacities were not proportional to the mass per area of each geotextile. Specific geotextile physical factors such as the diameter of the fibers and the tightness of the weave likely influenced retention capacity. For example, the medium black and thin white geotextiles had a noticeably looser weave than the thin black and thick black geotextiles, which likely effected how oil wetted the geotextile.

Figure 43 provides a comparison of the retention capacities of diesel and crude oil for each oleophilic material along with error bars that show the minimum and maximum retention capacities for each material. All points lie beneath the 1:1 dotted line except for the medium black geotextile. This shows that the medium black geotextile had a greater affinity for diesel while the other materials had a greater affinity for crude oil.

The data from these tests can be used to forecast the loading capacity of OBBs in several environments. Additionally, these results can help in identifying an oleophilic candidate material to use at a given site based on factors such as oil loading rates (if known) and type of oil present. However, these oil retention studies do not consider important factors that affect the required OBB retention capacity in the field like microbial activity, underlying soil composition and chemistry, OBB deterioration due to environmental factors, gas migration during tidal cycles, or preventing the geonet component of the GDL from the infiltration of fines. Therefore, site specific criteria should be considered when selecting an oleophilic material for an OBB.

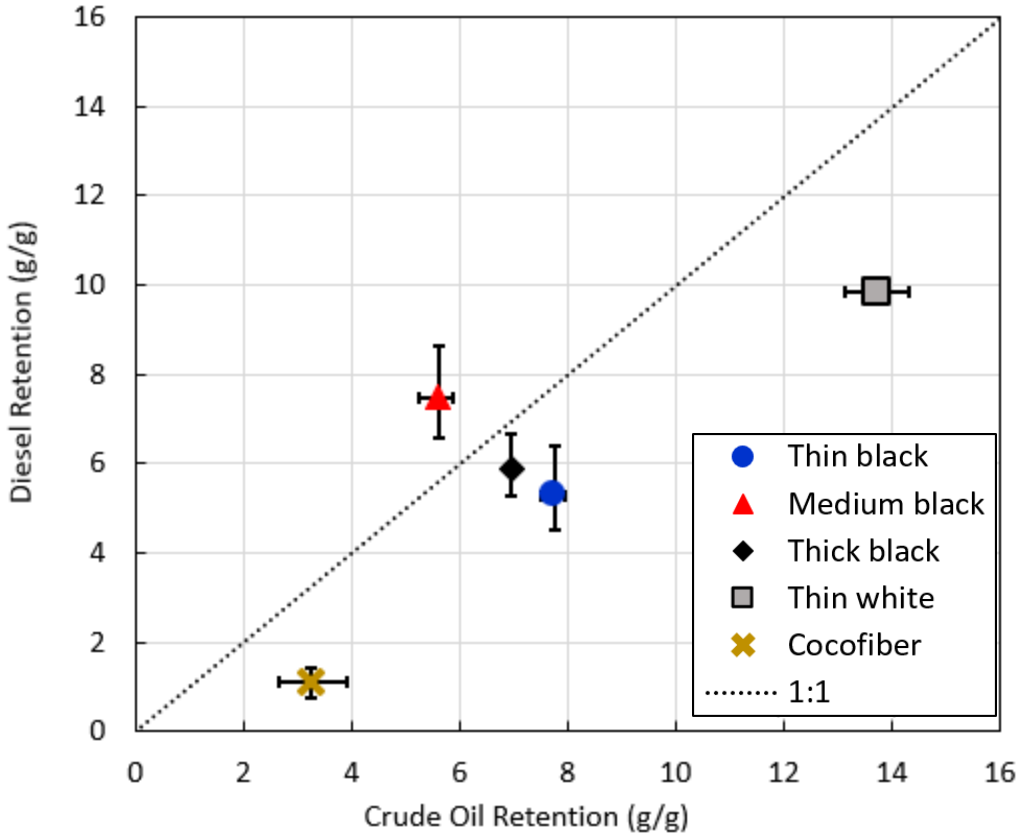

Figure 43. 1:1 plot comparing oleophilic material mass-per-mass retention of diesel and crude oil in dip test.

6. OIL DEGRADATION IN AN OLEOPHILIC BIO-BARRIER

6.1. Introduction

The purpose of an OBB is to facilitate the degradation of oil. The goal of this chapter is to provide a rough estimate of the degradation of oil at a site with an OBB versus a site with a traditional sorptive barrier. To distinguish the attenuation capacities between these barriers, both aerobic and anaerobic oil degradation rates were derived from oil landfarming literature and combined with OBB properties and observations described in (Chalfant 2015; Campbell 2017; Tochko 2018) and Chapters 3 – 5 of this study.

6.2. Background and Results

Landfarming is a widely used soil remediation technique in which contaminated soil is spread across a plot of land at a thickness typically between 0.3 m and 1 m (Paudyn et al. 2008). Mixing and tilling the contaminated soil as well as the addition of nutrients is common to expedite remediation as shown in Figure 44. Several oil landfarming case studies report degradation rate constants, and many more report total petroleum hydrocarbon (TPH) removal over a specific time period.

For this study, only non-nutrient amended landfarming studies were considered. Only plots that were regularly tilled were considered for aerobic degradation conditions, and control plots (plots that were not amended in any way) were considered for anaerobic degradation conditions. Rate constants were collected from eight studies, of which five studies included at least one aerated landfarming plot, while seven included at least one

control plot (Balba 1998; Hejazi and Husain 2004; Paudyn et al. 2008; Besalatpour et al. 2009; Wang et al. 2016; Brown et al. 2017; Guarino et al. 2017; Ortega et al. 2018).

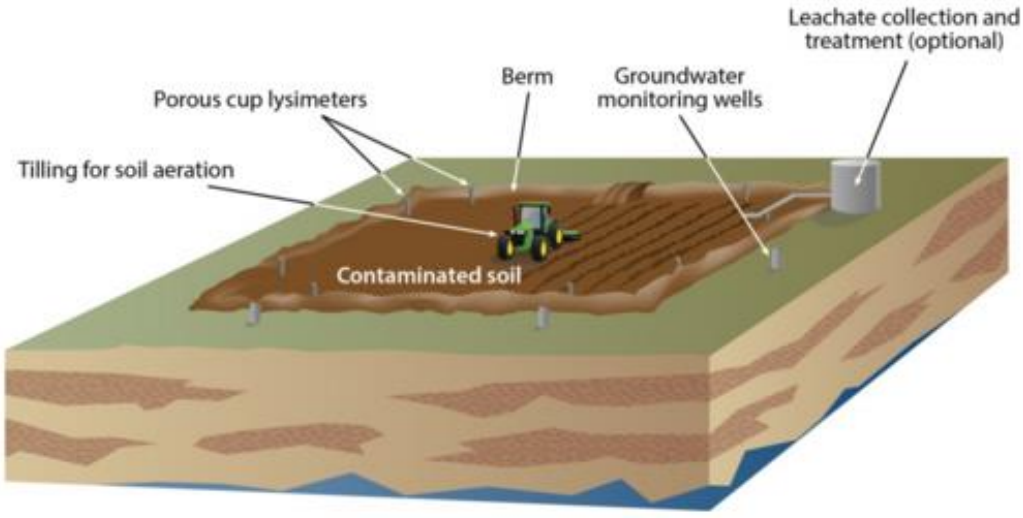

Figure 44. Landfarming diagram (from USEPA 1994).

Of the studies that reported TPH removal instead of a rate constant, first order degradation kinetics were assumed to calculate rate constants due to the routine use of first order kinetics in landfarming literature for oil degradation (Marin et al. 2005; Paudyn et al. 2008; Wang et al. 2016; Brown et al. 2017). For studies with multiple aerated or control landfarming plots, rate constants calculated for all aerobic and anaerobic plots were averaged respectively to yield one aerobic and one anaerobic rate constant per study. Then, the rate constants obtained from each study were average for both aerobic and anaerobic conditions. The settled upon rate constants were 0.009 day^{-1} for aerobic conditions ($k_{Aerobic}$) and 0.004 day^{-1} for anaerobic conditions ($k_{Anaerobic}$). The range of rate constants from the studies considered ranged from 0.005 day^{-1} to 0.017 day^{-1} in aerobic landfarming plots and 0.0001 day^{-1} to 0.014 day^{-1} in anaerobic landfarming plots. Tables 1 and 2 summarize the average aerobic and anaerobic rate constants from the studies

considered. Tables A2 and A3 in Appendix B show all rate constant values included in this study.

Table 1. Average aerobic rate constants.

Publication	Average Rate Constant, k (day^{-1})
Balba et al. 1998	0.0055
Besalatpour et al. 2009	0.007
Hejazi and Husain 2004	0.0075
Marin et al. 2005	0.009
Paudyn et al. 2008	0.016
Average	**0.009**
Standard Deviation	0.004
Minimum	0.005
Maximum	0.017

Table 2. Average anaerobic rate constants.

Publication	Average Rate Constant, k (day^{-1})
Balba et al. 1997	0.0006
Besalatpour et al. 2009	0.001
Wang et al. 2017	0.0028
Brown et al. 2017	0.0031
Ortega et al. 2018	0.0036
Hejazi and Husein 2004	0.004
Guarino et al. 2017	0.0061
Paudyn et al. 2008	0.007
Average	**0.004**
Standard Deviation	0.002
Minimum	0.0001
Maximum	0.014

While site specific factors will ultimately govern the total attenuation capacity at a given site, these aerobic and anaerobic rate constants can be plugged into a simple model to approximate the degradation in an OBB. Equation 1 is a first order kinetics equation

that splits the exponential term into two parts based on the assumption that the OBB is aerobic for some fraction of a day ($f_{Aerobic}$), anaerobic for the rest of the day ($1 - f_{Aerobic}$), and time, t, is equal to one day.

$$V_t = V_0 * e^{-k_{Anaerobic}*(1-f_{Aerobic})*t} * e^{-k_{Aerobic}*f_{Aerobic}*t} \quad (1)$$

A typical oil loading rate of 15 L of oil/m-yr (0.041 L/m-d) from Tochko (2018) was applied, where the unit "m" refers to a one meter length of shoreline. The initial volume of oil retained on the GDL component of the OBB per meter of shoreline, V_0 (L/m), on day one is assumed to equal the daily loading rate of 0.041 L/m. The final volume of oil retained on the GDL per meter of shoreline, V_t (L/m), is then calculated using Equation 1. On any given day, the initial volume on the GDL, V_0, is determined by adding the V_t for the previous day to the daily oil loading of 0.041 L/m-day.

The GDLs used in previous OBB installations (Chalfant 2015; Tochko 2018) and in the OBB described in Chapter 3 were manufactured to an area of 9.3 m by 3.8 m. The GDL installed in the OBB in Chapter 3 had the 9.3 m length side of the GDL oriented perpendicular to the shoreline. These dimensions and orientation are assumed for the OBB in the model described in this chapter. However, even loading is not expected in heterogeneous natural environments with preferential flow paths. For this model, only 20% of the OBB area was assumed to be wetted by oil, or 1.86 m^2 of oil wetted GDL per meter of shoreline. This percentage is based on field observations by Chalfant (2015) in which oil was determined to wet only 20% and 35% of field GDLs. In Equation 2, the fraction of a GDL area wetted by oil, $f_{GDL\_effective}$, is multiplied by the GDL area per meter

of shoreline, A_{GDL} (m^2/m), to calculate the effective area of a GDL per meter length of shoreline, $A_{GDL\_effective}$ (m^2/m).

$$A_{GDL\_effective} = A_{GDL} * f_{GDL\_effective} \quad (2)$$

After a four year OBB field trial at an oil impacted site, Tochko (2018) measured no detectable diesel range organics (DRO) 0 cm to 10 cm beneath the GDL and DRO concentrations in the low 1000s of mg/kg range 10 cm to 20 cm beneath the GDL. Oil composition analysis also suggested oil 10 cm to 20 cm beneath the GDL had been oxygenated. These results demonstrate the ability of an OBB to deliver oxygen to underlying sediments. To better estimate oil degradation as a result of increased oxygen delivery, the model incorporates an "aerobic sediment depth", $D_{Aerobic}$ (m), which is assumed to be 0.2 m. This estimate of aerobic sediment depth is based on observations from the destructive OBB analysis performed by Tochko (2018) and substantiated by Lukić et al. (2017) in a landfarming application who state that atmospheric oxygen diffusion needed for bioremediation in most soils can only be achieved at depths less than 0.3 m. The mass of aerobic soil per meter length of shoreline, $M_{Aerobic\_soil}$ (kg/m), is calculated using Equation 3, where ρ_b is the soil's bulk density in kg/m^3. The volume of oil in the aerobic soil, $V_{Oil\_in\_soil}$ (L/m), is estimated using Equation 4, where C (mg/kg) is the constant concentration of TPH in the aerobic soil, and ρ_{Oil} (mg/L) is the density of the oil. Finally, the volume of oil degraded in the aerobic soil per meter of shoreline per day, V_{Soil_deg} (L/m-day), can be calculated using Equation 5.

$$M_{Aerobic\_soil} = D_{Aerobic} * A_{GDL} * \rho_b \quad (3)$$

$$V_{Oil\_in\_soil} = \frac{M_{Aerobic\_soil} * C}{\rho_{Oil}} \quad (4)$$

$$V_{Soil\_deg} = V_{Oil\_in\_soil} * e^{-k_{Anaerobic}*(1-f_{Aerobic})*t} * e^{-k_{Aerobic}*f_{Aerobic}*t} \quad (5)$$

Figures 45 and 46 provide a graphical comparison of the required sorption capacities of an OBB and an RCM to the retention capacities of various oleophilic sorptive materials based on results from the dip test in Chapter 5 of this study (values were doubled to account for the two layers of geotextile on a GDL), and from values reported by Chalfant (2015) and substantiated by Tochko (2018), who both determined the retention capacity of a GDL with medium black geotextiles to be 3 L of diesel per m^2 of GDL. The traditional oil sorption barrier in the model is assumed to be an RCM. The retention capacity of an RCM was calculated to be approximately 4.8 L/m^2 and is based on the organoclay oil adsorption capacity reported in the CETCO Organoclay RCM datasheet. If the required retention capacity calculated by the model (indicated by a solid red line) exceeds the retention capacity of an oleophilic material, breakthrough occurs for that oleophilic material.

As shown in Figure 45, the sediments beneath the RCM are assumed to be anaerobic (oil in this zone will degrade anaerobically), and oil sorbed to the RCM is assumed to degrade at a negligible rate (i.e., zero degradation) due to binding of the oil onto the organoclay limiting microbial accessibility. Therefore, the RCM loads consistently until breakthrough occurs after approximately 218 days. Additionally, the cumulative volume of oil degraded is presented in Figure 45 for the 0.2 m of anaerobic sediments beneath the RCM (equivalent to the 0.2 m aerobic sediment depth in an OBB).

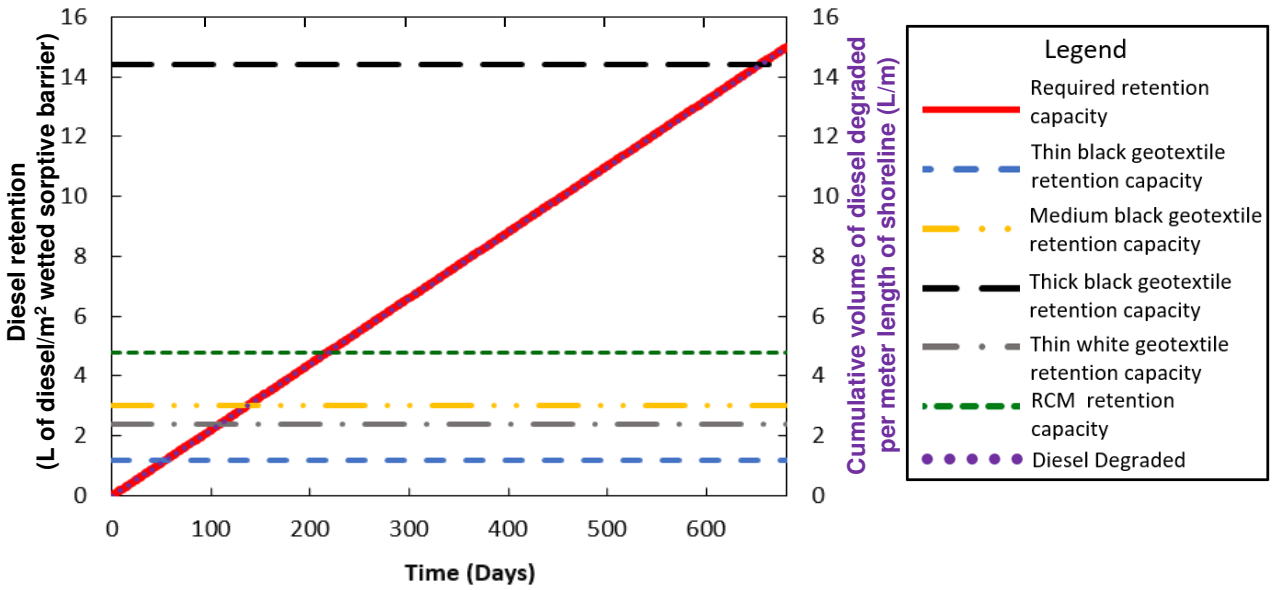

Figure 45. Required retention capacity of an RCM sorptive cap (L/m^2) at a typical oil-impacted GSI compared to the retention capacities of various oleophilic sorptive materials (primary y-axis) and cumulative volume of diesel degraded in the cap (secondary y-axis) over time.

Ideally, an OBB would create sustained aerobic conditions at all times, so $f_{Aerobic}$ would be 1. For field OBB monitoring study described in Chapter 3, the OBB maintained aerobic conditions except in the hours and days immediately following a precipitation event where redox conditions would temporarily drop to ORP values correlated with the nitrate/nitrite redox couple. However, these temporary drops in ORP were short-lived and typically returned to aerobic conditions within 12-24 hours. To account for this ORP behavior, $f_{Aerobic}$ in Figure 46 is estimated to be 0.9. Figure 46 shows that modifying only one parameter ($f_{Aerobic}$) significantly reduced the necessary retention capacity of the GDL as estimated by the model. The required retention capacity for the GDL in Figure 46 levels off at 2.6 L/m^2. Therefore, all of the oleophilic materials considered would provide sufficient protection against oil sheens except for a GDL with thin black or thin white geotextiles. Additionally, the cumulative volume of diesel degraded for an OBB is nearly

four-times greater than for the 0.2 m of anaerobic sediment below the RCM over the same time period.

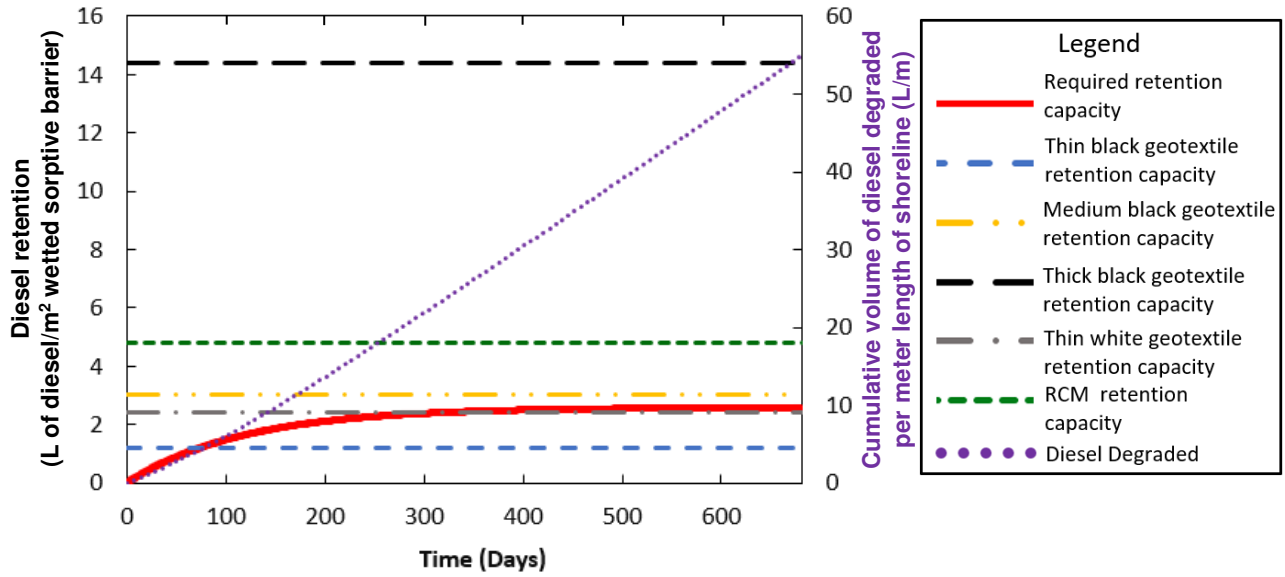

Figure 46. Required retention capacity of a GDL (L/m^2) compared to the retention capacities of various oleophilic sorptive materials (primary y-axis) and cumulative volume of diesel degraded in the OBB (secondary y-axis) over time.

Table 3. Summary of model parameters used in analysis (Note: $f_{Aerobic}$ = 0 and Aerobic Sediment Depth = 0 m for the model outputs displayed in Figure 45).

k(Aerobic) (1/day)	0.009
k(Anaerobic) (1/day)	0.004
Loading Rate (L Diesel/day)	0.041
Shore length (m)	1
GDL Width (m)	9.3
A_{GDL} (m^2/m)	9.3
$f_{GDL\_effective}$	0.2
$A_{GDL\_effective}$ (m^2/m)	1.86
$f_{Aerobic}$	0.9
e^-$k_{Aerobic}$*$f_{Aerobic}$*t	0.9919
e^-$k_{Anaerobic}$*(1-$f_{Aerobic}$)*t	0.9996
Soil Bulk Density (kg/m^3)	1680
Aerobic Sediment Depth (m)	0.2
Volume of Aerobic Soil (m^3/m)	1.86
Mass of Aerobic Soil (kg/m)	3124.8
Diesel Concentration in Aerobic Soil (mg/kg)	1500

Density of Diesel (kg/m^3)	850.8
Volume Diesel in Aerobic Soil (L/m)	5.509
Volume Degraded per Day (L Diesel/m-day)	0.0466
GDL Retention Capacity with Thin Black Geotextiles (L/m^2)	1.2
GDL Retention Capacity with Medium Black Geotextiles (L/m^2)	3
GDL Retention Capacity with Thick Black Geotextiles (L/m^2)	14.4
GDL Retention Capacity with Thin White Geotextiles (L/m^2)	2.4
RCM Retention Capacity (L/m^2)	4.8

While an OBB can be a sustainable solution for the prevention of surface water sheens at a GSI, site specific factors may necessitate more robust prevention strategies when loading is heavy. The model described in this section provides the framework to determine whether an OBB will provide sufficient protection against surface water oil sheens.

The application of land farming rate constants to this model has several limitations. Most notably, the oil impacted sediments in a landfarming plot do not experience the twice daily flooded periods that an OBB would experience in a tidal GSI. Nutrient amended landfarming plots may more accurately represent the nutrient delivery experienced by an OBB at a tidal GSI. Additionally, aeration of a landfarming plot due to tilling may not accurately represent the oxygen delivery in an OBB. Therefore, the oil degradation rate constants used for this model should only be considered to be approximations. To increase the accuracy and practicality of this model, parameters should be measured or estimated on a site by site basis. Additional research should be conducted to further understand the degradation kinetics in an OBB, and to estimate the fraction of a GDL that retains oil under different site conditions.

7. SUMMARY & CONCLUSION

Oleophilic bio-barriers (OBBs) catch and retain oil while simultaneously facilitating biodegradation through cyclic delivery of oxygen and nutrients via tidally driven water level fluctuations. Internet of Things (IoT) connected ORP sensors were installed in an OBB and verified the sustained oxidizing conditions of the system. Moreover, ORP monitoring can help detect imminent OBB failure and trigger a response before an OBB overloads and oil sheens are formed.

While an OBB can provide protection against the formation of surface water oil sheens at a tidal fluctuating GSI, site specific factors should be considered to decide whether an OBB is an appropriate solution. For example, large oil loading rates or sustained reducing conditions may necessitate alternative strategies. A preliminary model was developed to provide a framework to determine whether an OBB will provide sufficient protection against surface water oil sheens depending on model outputs and site specific environmental factors.

Several experiments prepared for this thesis were cut short because of lab closures due to COVID-19 limiting access to Colorado State University's Engineering Research Center (ERC). Appendix A focuses on the next steps to complete those experiments as well as recommendations for future work.

REFERENCES

Abbasian, F., Lockington, R., Mallavarapu, M. and Naidu, R. 2015. “A Comprehensive Review of Aliphatic Hydrocarbon Biodegradation by Bacteria.” Applied Biochemistry and Biotechnology 176(3):670–99.

Askarani, K., Stockwell, E., Piontek, K., & Sale, T. (2018). Thermal Monitoring of Natural Source Zone Depletion. Groundwater Monitoring & Remediation, 38(3), 43-52. https://doi.org/10.1111/gwmr.12286

Askarani, K., & Sale, T. (2020). Thermal estimation of natural source zone depletion rates without background correction. Water Research, 169, 115245. https://doi.org/10.1016/j.watres.2019.115245

Atlas, R. 1981. Microbial Degradation of Petroleum Hydrocarbons: An Environmental Perspective. Vol. 45.

Balba, M. 1998. “Methods Bioremediation of Oil-Contaminated Soil : Microbiological Methods for Feasibility Assessment and Field Evaluation.” 32:155–64.

Banks, M., C. Clennan, W. Dodds, and C. Rice. 1999. “Variations in Microbial Activity Due to Fluctuations in Soil Water Content at the Water Table Interface.” Journal of Environmental Science and Health - Part A Toxic/Hazardous Substances and Environmental Engineering 34(3):479–505.

Besalatpour, A., Hajabbasi, M., Khoshgoftarmanesh, A., and Dorostkar, V. 2009. “Bioremediation of Petroleum-Contaminated Soil Using Landfarming Technique : Influence on Soil Biological and Chemical Properties.” 1415–20.

Brauner, J. and Widdowson, M. 1997. “Sequential Electron Acceptor Model for Evaluation of in Situ Bioremediation of Petroleum Hydrocarbon Contaminants in Groundwater.” Annals of the New York Academy of Sciences 829:263–79.

Brown, D., Okoro, S., van Gils, J., van Spanning, R., Bonte, M., Hutchings, T., Linden, O., Egbuche, U., Bye Bruun, K., and Smith, J. 2017. “Comparison of Landfarming Amendments to Improve Bioremediation of Petroleum Hydrocarbons in Niger Delta Soils.” Science of the Total Environment 596–597:284–92.

Campbell, C. 2017. “Effects of Capping Material on Longevity of Degradable Contaminants in Sediments.” MS Thesis. Colorado State University.

Chalfant, M. 2015. “Oleophilic Bio-Barriers (OBBS) for Control of Hydrocarbon Sheens at Groundwater-Surface Water Interfaces.” MS Thesis. Colorado State University.

Das, N. and Chandran, P. 2011. “Microbial Degradation of Petroleum Hydrocarbon Contaminants: An Overview.” Biotechnology Research International 2011:1–13.

DeAngelis, K., Silver, W., Thompson, A., and Firestone, K. 2010. “Microbial Communities Acclimate to Recurring Changes in Soil Redox Potential Status.” Environmental Microbiology 12(12):3137–49.

Dobson, R., Schroth, M., and Zeyer, J. 2007. “Effect of Water-Table Fluctuation on Dissolution and Biodegradation of a Multi-Component, Light Nonaqueous-Phase Liquid.” Journal of Contaminant Hydrology 94(3–4):235–48.

Essington, M. 2015. “Soil and Water Chemistry: An Integrative Approach.” Pp. 365–66 in Soil and Water Chemistry: An Integrative Approach. CRC Press.

Fiedler, S., Vepraskas, M. and Richardson, J. 2007. Soil Redox Potential: Importance, Field Measurements, and Observations. Vol. 94. Elsevier Masson SAS.

Goncharuk, V., Bagrii, V., Mel’nik, L., Chebotareva, R., and Bashtan, S. 2010. “The Use of Redox Potential in Water Treatment Processes.” Journal of Water Chemistry and Technology 32(1):1–9.

Guarino, C., Spada, V., and Sciarrillo, R. 2017. “Assessment of Three Approaches of Bioremediation (Natural Attenuation, Landfarming and Bioagumentation – Assistited Landfarming) for a Petroleum Hydrocarbons Contaminated Soil.” Chemosphere 170:10–16.

Hawkins, A. 2013. “Processes Controlling The Behavior of LNAPLS at Groundwater Surface Water Interfaces.” MS Thesis. Colorado State University

Hejazi, R. and Husain, T. 2004. “Landfarm Performance under Arid Conditions. Evaluation of Parameters.” Environmental Science and Technology 2457–69.

Hinchee, R. and Olfenbuttel, R. 2013. In Situ Bioreclamation: Applications and Investigations for Hydrocarbon and Contaminated Site Remediation. Stoneham, MA, USA: Reed Publishing.

Lukić, B., Panico, A., Huguenot, D., Fabbricino, M., van Hullebusch, E., and Esposito, G. 2017. “A Review on the Efficiency of Landfarming Integrated with Composting as a Soil Remediation Treatment.” Environmental Technology Reviews 6(1):94–116.

Marin, J., Hernandez, T., and Garcia, C. 2005. “Bioremediation of Oil Refinery Sludge by Landfarming in Semiarid Conditions: Influence on Soil Microbial Activity.” Environmental Research 98(2):185–95.

Ortega, M., Guerrero, D., García-Martínez, M., Bolonio, D., Llamas, J., Canoira, L., and Gallego, J. 2018. “Optimization of Landfarming Amendments Based on Soil Texture and Crude Oil Concentration.” Water, Air, and Soil Pollution 229(234)

Paudyn, K., Rutter, A., Kerry Rowe, R., and Poland, J., 2008. “Remediation of Hydrocarbon Contaminated Soils in the Canadian Arctic by Landfarming.” Cold Regions Science and Technology 53(1):102–14.

Reddy, K. and DeLaune. R. 2008. Biogeochemistry of Wetlands: Science and Applications. CRC Press.

Sale, T., Hopkins, H., and Kirkman, A. 2018. “Managing Risk at LNAPL Sites Frequently Asked Questions.” American Petroleum Institute Tech Bulletin.

Striggow, B. 2017. Field Measurement of Oxidation-Reduction Potential (ORP).

Tochko, L. 2018. “Processes Governing the Performance of Oleophilic Bio-Barriers (OBBs) – LABORATORY AND FIELD STUDIES.” MS Thesis. Colorado State University.

VanLoon, G. and Duffy, S. 2011. Environmental Chemistry: A Global Perspective. 3rd ed. Oxford University Press.

Varjani, S. 2017. “Microbial Degradation of Petroleum Hydrocarbons.” Bioresource Technology.

Vilgalys, R. 2012. “Redox Ladder.” Duke University Microbial Ecology & Evolution. Retrieved May 20, 2020 (https://sites.duke.edu/microbialecology/class-glossary/).

Wang, S., Kuo, Y., Hong, A., Chang, Y., and Kao, C. 2016. “Bioremediation of Diesel and Lubricant Oil-Contaminated Soils Using Enhanced Landfarming System.” Chemosphere 164:558–67.

Widdel, F., Antje, B., and Ralf, R. 2006. “Anaerobic Biodegradation of Hydrocarbons Including Methane.” P. Volume 2; Pages 1028-1032 in The Prokaryotes; Third Edition; A Handbook on the Biology of Bacteria; Ecophysiology and Biochemistry, edited by M. Dworkin, S. Falkow, E. Rosenberg, K.-H. Schleifer, and E. Stackebrandt. Springer.

Yadav, B. and Hassanizadeh, S. 2011. “An Overview of Biodegradation of LNAPLs in Coastal (Semi)-Arid Environment.” Water, Air, and Soil Pollution 220(1–4):225–39.

Zimbron, J., Sale, T., Biondolillo, M., Batten, P., Chalfant, M., and Lyverse, M. 2014. “Oleophilic Bio-Barrier for Controlling NAPL Migration - United States Patent Number US20160075576A1.” 2(12).

APPENDIX A

A1. Next Steps

Several experiments prepared for this thesis were cut short because of COVID-19 limiting access to Colorado State University's Engineering Research Center (ERC). This section focuses on the necessary steps to complete these experiments.

A1.1. Geotextile Retention and Breakthrough of Diesel in Water

The diesel bubbling test described in Chapter 5 was meant to test the same non-woven geotextiles that were tested in the dip test. However, the medium black geotextile only underwent one trial in the diesel bubbling test and needs to be tested at least three more times. The procedure to perform these tests is as follows:

1. Cut out a "medium black" (13.4 oz/m^2) geotextile disk to fit the inner diameter of a 1000 mL Pyrex beaker (about 10 cm).
2. Suspend the geotextile disk at 700 mL mark of the beaker and apply caulk around the edges (this may require several caulk appliances to create a seal).
3. Once the caulk is set and liquid is no longer able to escape around the outside of the geotextile, the beaker should be filled with tap water to the 800 mL mark of the beaker.
4. Record the volume of diesel in the syringe and begin the experiment.
5. Slowly and simultaneously inject diesel and air into the beaker so air bubbles are surrounded by diesel as the intermediate wetting fluid (The experiment should be performed in the dark with a UV light, so that the diesel fluoresces, and sheens are easier to detect).

6. The experiment is over when a visible sheen is formed on the water surface and the final volume of diesel in the syringe is recorded.

A1.2. Functional Versus Failed OBB Sand Tank Experiment

After deconstructing the lab OBB monitoring experiment described in Chapter 4, a side by side OBB monitoring experiment was set up in the sand tank. One half of the tank had a GDL between layers of coarse sand and overlying a layer of fine sand as shown in Figure 1A(a). The other half of the tank was set up in the same way except the geonet component of the GDL was packed with fatty clay collected from a deposit just south of the ERC. The side of the sand tank with the failed GDL was meant to simulate OBB failure by means of sedimentation and is herein referred to as “failed OBB”. Sixteen ORP sensors were split between the two halves of the sand tank and were arranged to differentiate the ORP in a functional OBB versus a failed OBB and to best visualize the effect of water level on the oxygen delivery capabilities of an OBB.

The sand tank was operated for about two weeks and ORP values were similar except for the ORP inside the GDL, which was substantially lower in the failed OBB. By resuming daily drain/fill cycles, the ORP values in the functional OBB are expected to be significantly greater than the ORP values in the failed OBB, demonstrating the ability for a properly functioning GDL to create a more oxidizing environment.

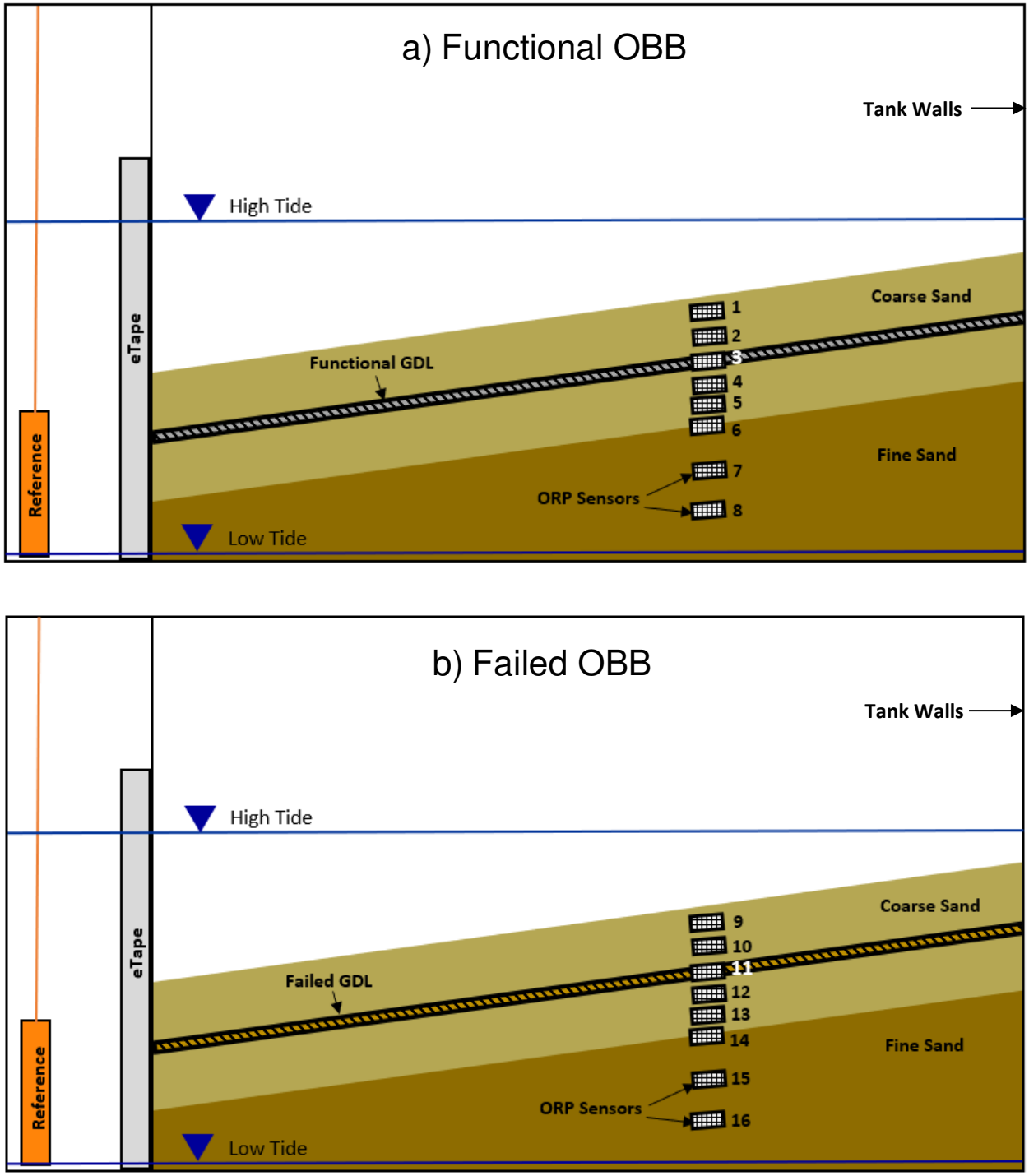

Figure A1. (a) Functional OBB versus (b) failed OBB sand tank setup diagram.

The procedure to resume the experiment is as follows:

1. Power on all pumps connected to the sand tank OBB to resume daily drain/fill cycles (Influent and effluent pumps are connected to automatic timers which turn the influent pump on and the effluent pump off at 1 PM, then turn the effluent pump on and the influent pump off at 1 AM).
2. Plug in the data logger mounted to the top of the sand tank. Once data loggers are plugged back in, data will automatically be collected and sent to Ubidots every five minutes. The data will be sent to the Center for Contaminant Hydrology (CCH) Ubidots account under the device name "Wes_Sand_Tank_ORP". The device is registered under the CCH Particle account.

A2. Future Work

While Chapter 6 of this study provides the framework for estimating oil degradation in an OBB, future research will be necessary to further correlate ORP with the rates of natural attenuation. To be conservative, the rate constants used in this study were from non-nutrient amended landfarming studies. However, the constant delivery of oxygen and nutrients to an OBB in a tidal setting may create an environment more comparable to nutrient and fertilizer amended landfarming plots. Ideally, future work would focus on degradation rates in an OBB, so oil degradation estimates do not rely on rate constants from land farming publications, and instead are based on empirical data.

Installing an OBB in a non-tidal setting may also be beneficial in sheen prevention and soil remediation. While oxygen and nutrient delivery would not be tidally driven,

oxygen and nutrients as well as other chemical oxidants could be pumped into the subsurface via the GDL's geonet, which could enhance bioremediation.

In previous OBB field studies, the OBB was successful in preventing surface water oil sheens (Chalfant 2015; Tochko 2018). However, these OBBs were installed in environments with low loading rates. Future research should study OBB performance in a wider range of site conditions. For sites with high oil loading rates, multiple layers of GDL or geotextile could increase protection against sheening. Additional sheen prevention strategies can be combined with OBBs such as the addition of an RCM to an OBB as described in Chapter 3.

APPENDIX B

B1. Data Tables

B1.1. OBB Degradation Model

Table A1. Average landfarming aerobic oil degradation rate constants with publication notes.

Aerobic		
Publication	Rate Constant, k (day^{-1})	Notes
Marin et al. 2005	0.009	Aerated once a month. Oil refinery sludge contaminated soil. 11 month trial. 19 degrees C average. 5-6% TPH w/w. 1m depth. Sludge additions in months 1,3,5,7,9 and 11.
Paudyn et al. 2008	0.016	Diesel contaminated soil, average summer soil temperature of 9.3°C, 0.3m depth, initial TPH~2800mg/kg.
Besalatpour et al. 2009	0.007	Aerated every 3 days. Plots were irrigated near field capacity of 0.7.
Balba et al. 1998	0.0055	Aerated twice a week. "Oily sludge" possibly crude oil contaminated soil. 30cm depth. 3-4% TPH
Hejazi and Husain 2004	0.0075	Aerated once a week, concentrations were in terms of "Oil & Grease", these rate constants were calculated only during periods of degradation.
average	0.009	
Standard Deviation	0.004	

Table A2. All landfarming aerobic oil degradation rate constants with publication notes.

Publication	**Rate Constant, k (day^{-1})**	**Notes**
Besalatpour et al. 2009	0.007	Plot S1 at 2 months
Besalatpour et al. 2009	0.008	Plot S2 at 2 months
Besalatpour et al. 2009	0.006	Plot S1 at 4 months
Besalatpour et al. 2009	0.007	Plot S2 at 4 months
Average	0.007	
Balba et al. 1997	0.006	6 month k
Balba et al. 1997	0.005	12 month k
Average	0.0055	
Paudyn et al. 2008	0.017	Aerated daily.

Publication	Rate Constant, k (day^{-1})	Notes
Paudyn et al. 2008	0.015	Aerated every 4 days.
Average	0.016	
Marin et al. 2004	0.013	2 month k.
Marin et al. 2004	0.005	11 month k.
Average	0.009	
Hejazi and Husein 2004	0.008	Not irrigated.
Hejazi and Husein 2004	0.007	Irrigated.
Average	0.0075	

Table A3. All landfarming anaerobic oil degradation rate constants with publication notes.

Publication	Rate Constant, k (day^{-1})	Notes
Ortega et al. 2018	0.0001	Plot A1
Ortega et al. 2018	0.0005	Plot A2
Ortega et al. 2018	0.0003	Plot B1
Ortega et al. 2018	0.0004	Plot B2
Ortega et al. 2018	0.0002	Plot C1
Ortega et al. 2018	0.0010	Plot C2
Average	0.0004	
Guarino et al. 2017	0.0140	Lot 2 at 60 days. 0-1.5m depth.
Guarino et al. 2017	0.0090	Lot 2 at 90 days. 0-1.5m depth.
Guarino et al. 2017	0.0010	Lot 2 at 60 days. 1.5-3m depth.
Guarino et al. 2017	0.0060	Lot 2 at 90 days. 1.5-3m depth.
Guarino et al. 2017	0.0050	Lot 4 at 60 days. 0-1.5m depth.
Guarino et al. 2017	0.0050	Lot 4 at 90 days. 0-1.5m depth.
Guarino et al. 2017	0.0070	Lot 4 at 60 days. 1.5-3m depth.
Guarino et al. 2017	0.0060	Lot 4 at 90 days. 1.5-3m depth.
Guarino et al. 2017	0.0030	Lot 5 at 60 days. 0-1.5m depth.
Guarino et al. 2017	0.0040	Lot 5 at 90 days. 0-1.5m depth.
Guarino et al. 2017	0.0040	Lot 5 at 60 days. 1.5-3m depth.

Publication	Rate Constant, k (day^{-1})	Notes
Guarino et al. 2017	0.0090	Lot 5 at 90 days. 1.5-3m depth.
Average	0.0061	
Wang et al. 2017	0.0039	Initial ORP = 245 mV, 80 day k.
Wang et al. 2017	0.0017	175 day k.
Average	0.0028	
Besalatpour et al. 2009	0.0010	Plot S1 at 2 months.
Besalatpour et al. 2009	0.0010	Plot S2 at 2 months.
Besalatpour et al. 2009	0.0010	Plot S1 at 4 months.
Besalatpour et al. 2009	0.0008	Plot S2 at 4 months.
Average	0.0010	
Balba et al. 1997	0.0006	6 month k
Balba et al. 1997	0.0006	12 month k
Average	0.0006	

Table A4a. Part 1 of OBB degradation model days 0-10 spreadsheet output.

Day	Volume/Area (L Diesel /m^2 Oleophilic Material)	Initial Volume (L Diesel)	Volume After Degradation (L Diesel)	Rate of Disappearance on Oleophilic Material (L Diesel/day)
0	0	0	0	0
1	0.022	0.041	0.041	0.0005
2	0.043	0.082	0.081	0.0009
3	0.065	0.122	0.120	0.0014
4	0.086	0.161	0.159	0.0019
5	0.106	0.200	0.198	0.0023
6	0.127	0.239	0.236	0.0028
7	0.147	0.277	0.274	0.0032
8	0.167	0.315	0.311	0.0037
9	0.187	0.352	0.348	0.0041
10	0.207	0.389	0.385	0.0045

Table A4b. Part 2 of OBB degradation model days 0-10 spreadsheet output.

Cumulative Volume Degraded on Oleophilic Material (L Diesel)	Cumulative Volume Degraded on Oleophilic Material and in Underlying Aerobic Sediment (L Diesel)
0	0
0.0005	0.0646
0.0014	0.1296
0.0028	0.1951
0.0047	0.2610
0.0070	0.3275
0.0098	0.3943
0.0130	0.4616
0.0167	0.5294
0.0208	0.5975
0.0253	0.6662

B1.2. Dip Test Data

Table A5a. Part 1 of dip test data.

Area (in^2)	Material	Oil	Soak Time (min)	Drip time (min)	Dry mass (g)	Wet mass (g)	Mass retained (g)
9	Coco fiber mat	Diesel	5	1	3.330 (with tray)	7.513 (with tray)	4.183
	Coco fiber braid (~1/2" thick)	Diesel	5	1	0.595	1.436	0.841
	Coco fiber braid (~1/2" thick)	Diesel	1	1	0.423	0.864	0.441
	Coco fiber braid	Diesel	5	1	0.349	0.619	0.27
	Coco fiber braid	Diesel	5	1	0.351	0.79	0.439
	Coco fiber braid	Diesel	5	1	0.24	0.48	0.24
	Coco fiber braid	Diesel	1	1	0.352	0.747	0.395
	Coco fiber braid	Diesel	1	1	0.303	0.646	0.343
3.69	Thin black geotextile	Diesel	2	3	0.56	3.33	2.77
3.69	Thin black geotextile	Diesel	2	5	0.54	3.07	2.53

Area (in^2)	Material	Oil	Soak Time (min)	Drip time (min)	Dry mass (g)	Wet mass (g)	Mass retained (g)
3.69	Thin black geotextile	Diesel	2	7	0.51	3.37	2.86
3.69	Thin black geotextile	Diesel	2	10	0.53	2.93	2.4
3.69	Thin black geotextile	Diesel	1	10	0.49	2.94	2.45
3.69	Thin black geotextile	Diesel	2	10	0.54	3.11	2.57
3.69	Thin black geotextile	Diesel	5	10	0.56	3.25	2.69
3.69	Thin black geotextile	Diesel	10	10	0.58	3.35	2.77
3.69	Thin black geotextile (0.5 kg compression)	Diesel	1	3	0.49	3.63	3.14
3.69	Thin black geotextile (1 kg compression)	Diesel	1	3	0.49	3.37	2.88
3.69	Thin black geotextile (2 kg compression)	Diesel	1	3	0.49	3.44	2.95
3.69	Thin black geotextile (3 kg compression)	Diesel	1	3	0.49	3.41	2.92
3.69	Medium black geotextile	Diesel	2	3	0.9	7.47	6.57
3.69	Medium black geotextile	Diesel	2	5	0.74	6.46	5.72
3.69	Medium black geotextile	Diesel	2	7	0.96	7.27	6.31
3.69	Medium black geotextile	Diesel	2	10	0.81	6.85	6.04
3.69	Medium black geotextile	Diesel	1	10	0.92	7.35	6.43
3.69	Medium black geotextile	Diesel	2	10	0.93	7.53	6.6
3.69	Medium black geotextile	Diesel	5	10	0.94	7.39	6.45
3.69	Medium black geotextile	Diesel	10	10	1	7.92	6.92
3.69	Medium black geotextile (0.5 kg compression)	Diesel	1	3	0.92	8.88	7.96

Area (in^2)	Material	Oil	Soak Time (min)	Drip time (min)	Dry mass (g)	Wet mass (g)	Mass retained (g)
3.69	Medium black geotextile (1 kg compression)	Diesel	1	3	0.92	8.84	7.92
3.69	Medium black geotextile (2 kg compression)	Diesel	1	3	0.92	8.15	7.23
3.69	Medium black geotextile (3 kg compression)	Diesel	1	3	0.92	8.03	7.11
3.69	Thick black geotextile	Diesel	2	3	2.71	18.88	16.17
3.69	Thick black geotextile	Diesel	2	5	2.66	17.96	15.3
3.69	Thick black geotextile	Diesel	2	7	2.47	18.9	16.43
3.69	Thick black geotextile	Diesel	2	10	2.73	17.77	15.04
3.69	Thick black geotextile	Diesel	1	10	2.52	15.79	13.27
3.69	Thick black geotextile	Diesel	2	10	2.3	17.58	15.28
3.69	Thick black geotextile	Diesel	5	10	2.49	17.08	14.59
3.69	Thick black geotextile	Diesel	10	10	2.22	16.16	13.94
3.69	Thick black geotextile (0.5 kg compression)	Diesel	1	3	2.67	18.43	15.76
3.69	Thick black geotextile (1 kg compression)	Diesel	1	3	2.67	17.99	15.32
3.69	Thick black geotextile (2 kg compression)	Diesel	1	3	2.67	17.68	15.01
3.69	Thick black geotextile (3 kg compression)	Diesel	1	3	2.67	17.46	14.79
3.69	Geocomposite (diamond geonet) (0.5 kg compression)	Diesel	1	3	5.27	18.02	12.75
3.69	Geocomposite (diamond geonet) (1 kg compression)	Diesel	1	3	5.27	18.04	12.77

Area (in^2)	Material	Oil	Soak Time (min)	Drip time (min)	Dry mass (g)	Wet mass (g)	Mass retained (g)
3.69	Geocomposite (diamond geonet) (2 kg compression)	Diesel	1	3	5.27	17.71	12.44
3.69	Geocomposite (diamond geonet) (3 kg compression)	Diesel	1	3	5.27	17.63	12.36
3.69	Geocomposite (square geonet) (0.5 kg compression)	Diesel	1	3	6.76	19.83	13.07
3.69	Geocomposite (square geonet) (1 kg compression)	Diesel	1	3	6.76	20.17	13.41
3.69	Geocomposite (square geonet) (2 kg compression)	Diesel	1	3	6.76	20.26	13.5
3.69	Geocomposite (square geonet) (3 kg compression)	Diesel	1	3	6.76	19.71	12.95
3.14	Thin white geotextile	Diesel	1	2	0.478	5.176	4.698
3.14	Thin white geotextile	Diesel	1	2	0.49	5.333	4.843
3.14	Thin white geotextile	Diesel	1	2	0.484	5.304	4.82
3.14	Thin white geotextile	Diesel	1	2	0.484	5.272	4.788
3.14	Thin white geotextile	Diesel	1	2	0.55	5.762	5.212
3.14	Thin white geotextile	Diesel	1	2	0.514	5.664	5.15
4.5	Coir mat	Diesel	1	2	2	4.285	2.285
4.5	Coir mat	Crude	1	2	2.525	12.18	9.655
	Coco fiber braid	Crude	1	2	0.454	1.783	1.329
	Coco fiber braid	Crude	1	2	0.287	1.251	0.964
	Coco fiber braid	Crude	1	2	0.325	1.323	0.998
	Coco fiber braid	Crude	1	2	0.385	1.408	1.023
	Coco fiber braid	Crude	1	2	0.233	1.108	0.875
	Coco fiber braid	Crude	1	2	0.188	0.921	0.733
	Coco fiber braid	Crude	1	2	0.396	1.623	1.227
3.14	Thin black geotextile	Crude	1	2	0.507	4.545	4.038

Area (in^2)	Material	Oil	Soak Time (min)	Drip time (min)	Dry mass (g)	Wet mass (g)	Mass retained (g)
3.14	Thin black geotextile	Crude	1	2	0.553	4.704	4.151
3.14	Thin black geotextile	Crude	1	2	0.503	4.423	3.92
3.14	Medium black geotextile	Crude	1	2	0.755	5.19	4.435
3.14	Medium black geotextile	Crude	1	2	0.753	5.054	4.301
3.14	Medium black geotextile	Crude	1	2	0.798	4.995	4.197
3.14	Thick black geotextile	Crude	1	2	2.023	15.936	13.913
3.14	Thick black geotextile	Crude	1	2	2.042	16.41	14.368
3.14	Thick black geotextile	Crude	1	2	2.183	17.334	15.151
3.14	Thin white geotextile	Crude	1	2	0.447	6.854	6.407
3.14	Thin white geotextile	Crude	1	2	0.492	6.953	6.461
3.14	Thin white geotextile	Crude	1	2	0.502	7.137	6.635
3.14	Thin white geotextile	Crude	1	2	0.522	7.951	7.429

Table A5b. Part 2 of dip test data.

Legend:

Mass retained per dry mass (g/g)	Mass retained per area (g/in^2)	Volume retained per area (L/m^2)	Dry mass per area (g/in^2)
1.413			
1.043			
0.774			
1.251			
1.000			
1.122			

Mass retained per dry mass (g/g)	Mass retained per area (g/in^2)	Volume retained per area (L/m^2)	Dry mass per area (g/in^2)
1.132			
4.95	0.75	1.37	0.15
4.69	0.69	1.25	0.15
5.61	0.78	1.41	0.14
4.53	0.65	1.18	0.14
5.00	0.66	1.21	0.13
4.76	0.70	1.27	0.15
4.80	0.73	1.33	0.15
4.78	0.75	1.37	0.16
6.41	0.85	1.55	0.13
5.88	0.78	1.42	0.13
6.02	0.80	1.46	0.13
5.96	0.79	1.44	0.13
7.30	1.78	3.24	0.24
7.73	1.55	2.82	0.20
6.57	1.71	3.12	0.26
7.46	1.64	2.98	0.22
6.99	1.74	3.17	0.25
7.10	1.79	3.26	0.25
6.86	1.75	3.18	0.25
6.92	1.88	3.42	0.27
8.65	2.16	3.93	0.25
8.61	2.15	3.91	0.25
7.86	1.96	3.57	0.25
7.73	1.93	3.51	0.25
5.97	4.38	7.98	0.73
5.75	4.15	7.55	0.72
6.65	4.45	8.11	0.67
5.51	4.08	7.43	0.74
5.27	3.60	6.55	0.68
6.64	4.14	7.54	0.62
5.86	3.95	7.20	0.67
6.28	3.78	6.88	0.60
5.90	4.27	7.78	0.72
5.74	4.15	7.56	0.72
5.62	4.07	7.41	0.72
5.54	4.01	7.30	0.72
2.42	3.46	6.29	
2.42	3.46	6.30	

Mass retained per dry mass (g/g)	Mass retained per area (g/in^2)	Volume retained per area (L/m^2)	Dry mass per area (g/in^2)
2.36	3.37	6.14	
2.35	3.35	6.10	
1.93	3.54	6.45	
1.98	3.63	6.62	
2.00	3.66	6.67	
1.92	3.51	6.39	
9.83	1.27	2.32	0.15
9.88	1.31	2.39	0.16
9.96	1.31	2.38	0.15
9.89	1.30	2.36	0.15
9.48	1.41	2.57	0.18
10.02	1.40	2.54	0.16
1.14	0.62	1.13	0.44
3.82	2.62	4.77	0.56
2.927			
3.359			
3.071			
2.657			
3.755			
3.899			
3.098			
7.964	1.286	2.26	0.16
7.506	1.322	2.33	0.18
7.793	1.248	2.20	0.16
5.874	1.412	2.48	0.24
5.712	1.370	2.41	0.24
5.259	1.337	2.35	0.25
6.877	4.431	7.80	0.64
7.036	4.576	8.05	0.65
6.940	4.825	8.49	0.70
14.333	2.040	3.59	0.14
13.132	2.058	3.62	0.16
13.217	2.113	3.72	0.16
14.232	2.366	4.16	0.17

B1.3. Diesel Bubbling Test Data

Table A6. Diesel bubbling test data.

Geotextile	Volume of diesel at breakthrough (mL)	Approximate fraction of diesel wetted area of geotextile	Retention at breakthrough (L/m^2)
Thin black	2.7	0.33	0.3
Thin black	2.2	0.25	0.3
Thin black	1.5	0.33	0.2
Thin black	1.5	0.25	0.2
Thin black	2.5	0.25	0.3
Thin black	2.8	0.2	0.3
Medium black	8.7	0.33	1.1
Medium black	Trials not completed		
Medium black			
Medium black			
Geotextile	**Volume of diesel at breakthrough (mL)**	**Approximate fraction of diesel wetted area of geotextile**	**Retention at breakthrough (L/m^2)**
Thick black	28	0.9	3.5
Thick black	23.5	0.75	2.9
Thick black	34.5	0.9	4.3
Thick black	32	0.9	3.9
Thin white	4	0.25	0.5
Thin white	4.3	0.25	0.5
Thin white	7	0.5	0.9
Thin white	5.3	0.33	0.7

APPENDIX C

C1. Diesel Bubbling Test Photos

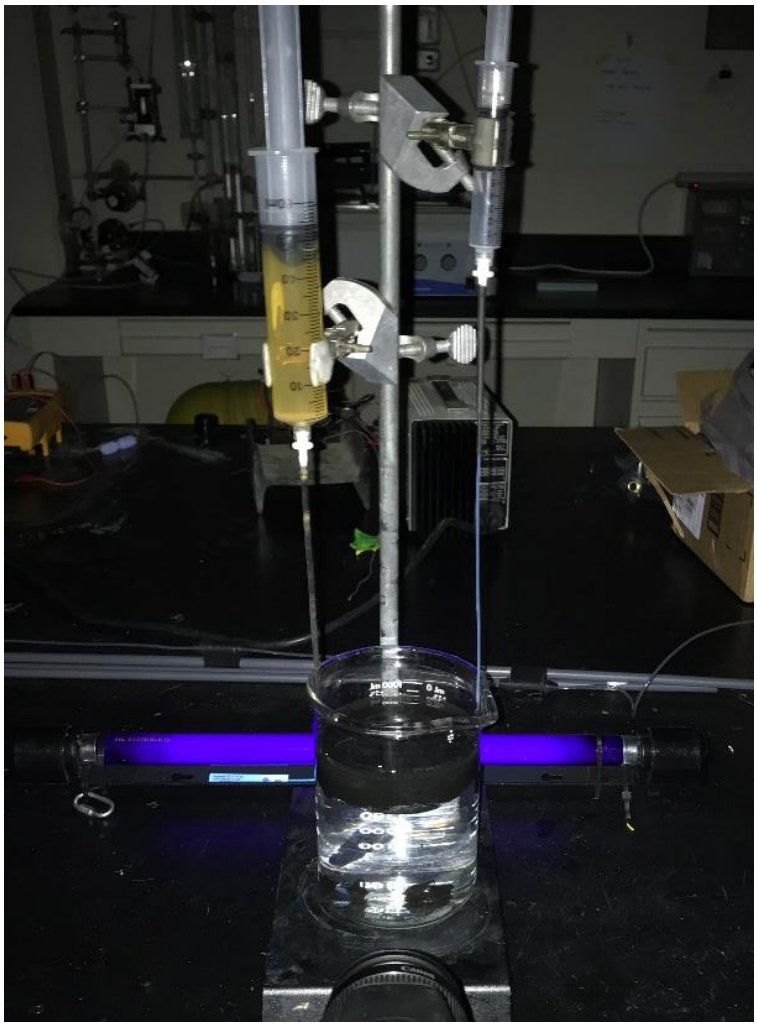

Figure A2. Photo of diesel bubbling test apparatus setup.

Figure A3. Photo of diesel and air tubing setup.

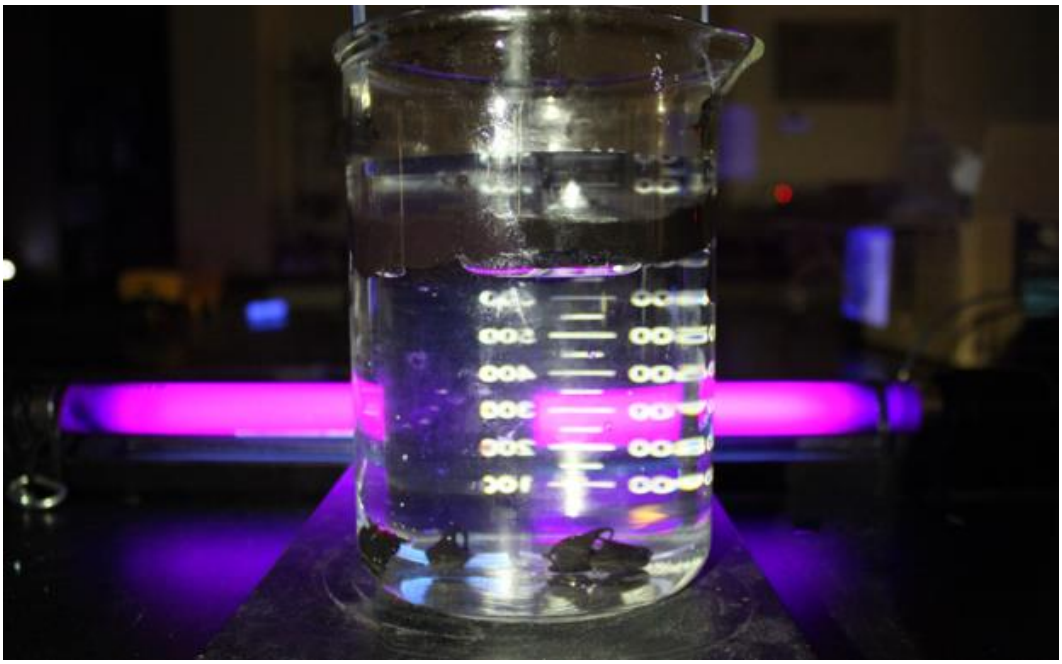

Figure A4. Photo of diesel bubbling test beaker setup.

Figure A5. Photo of trial 1 of the diesel bubbling test diesel sheen.

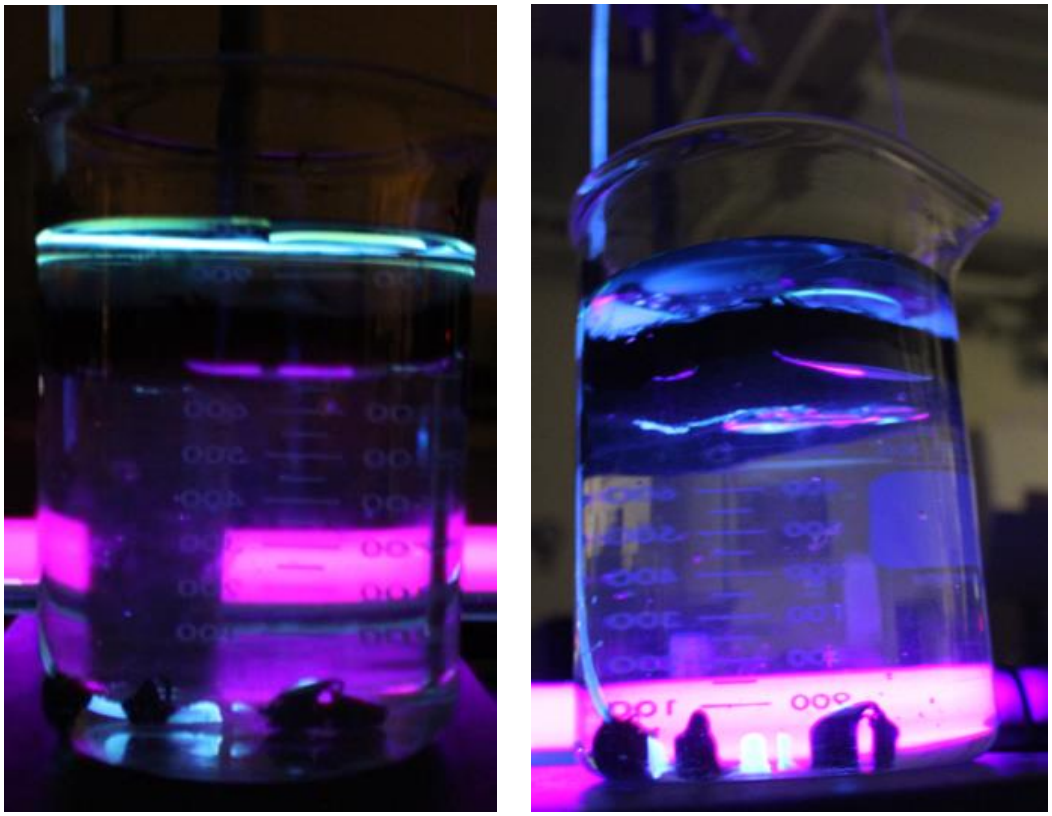

Figure A6. Photos of trial 1 diesel sheen a) side view and b) bottom view.

Figure A7. Photo of trial 10 thick black geotextile diesel sheen.

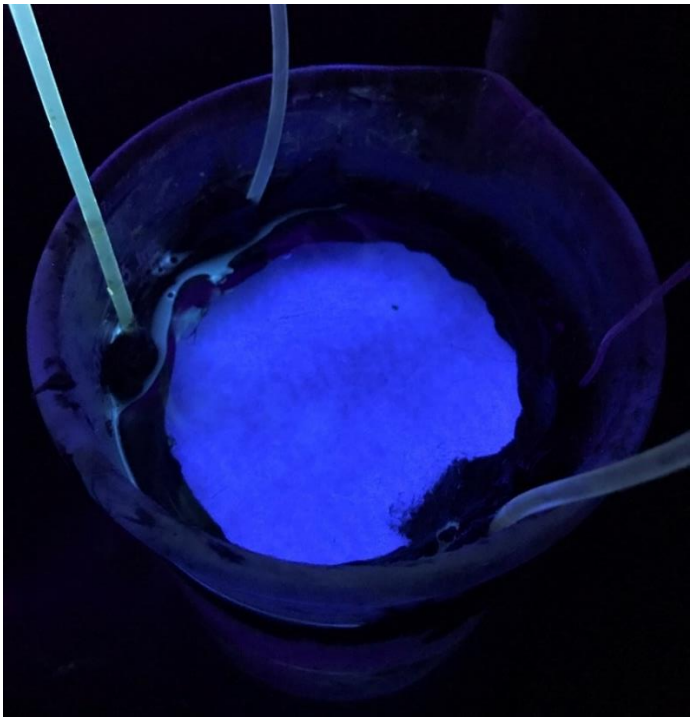

Figure A8. Photo of trial 11 thin white geotextile diesel sheen.

C2. Lab OBB Monitoring Experiment Photos

Figure A9. Photo of sand tank OBB gravel and geotextile layers.

Figure A10. Photo of sand tank geotextile caulk seal.

Figure A11. Photo of sand tank OBB sand/bentonite seal.

Figure A12. Photo of sensor “O” installation in sand tank OBB fine sand.

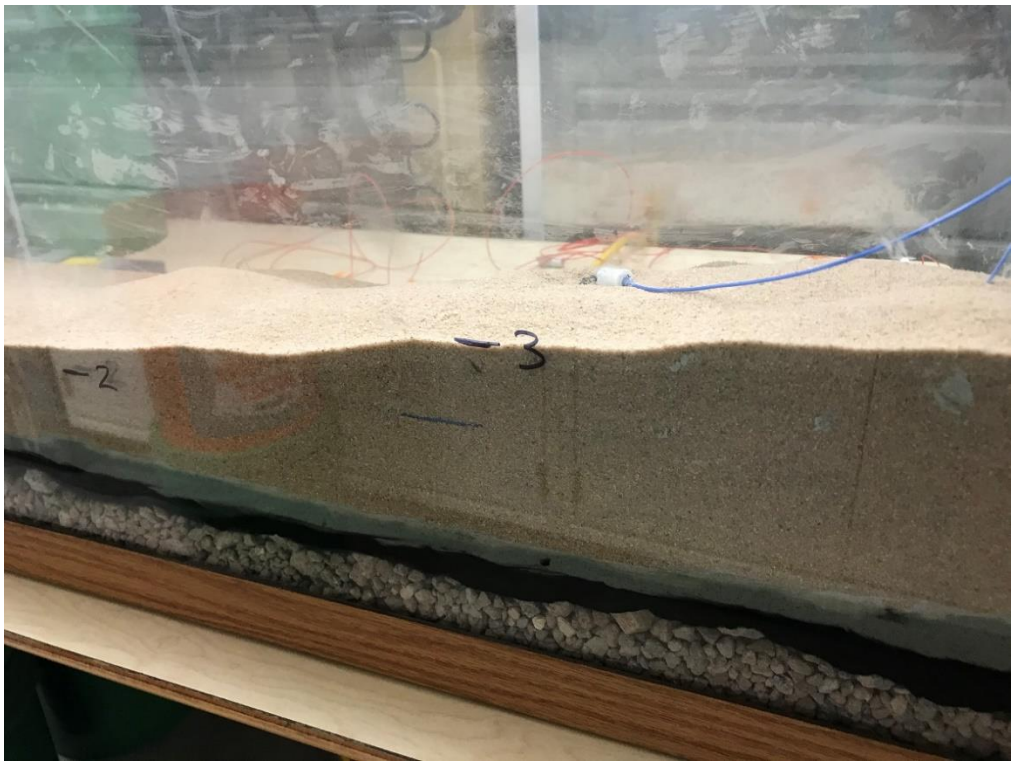

Figure A13. Photo of sensor “P” installation in sand tank OBB fine sand.

Figure A14. Photo of sand tank OBB coarse sand layer installation.

Figure A15. Photo of ORP sensor being inserted into GDL.

Figure A16. Photo of ORP sensor embedded in GDL.

Figure A17. Photo of GDL installation in sand tank OBB.

Figure A18. Photo of GDL caulk seal in sand tank OBB.

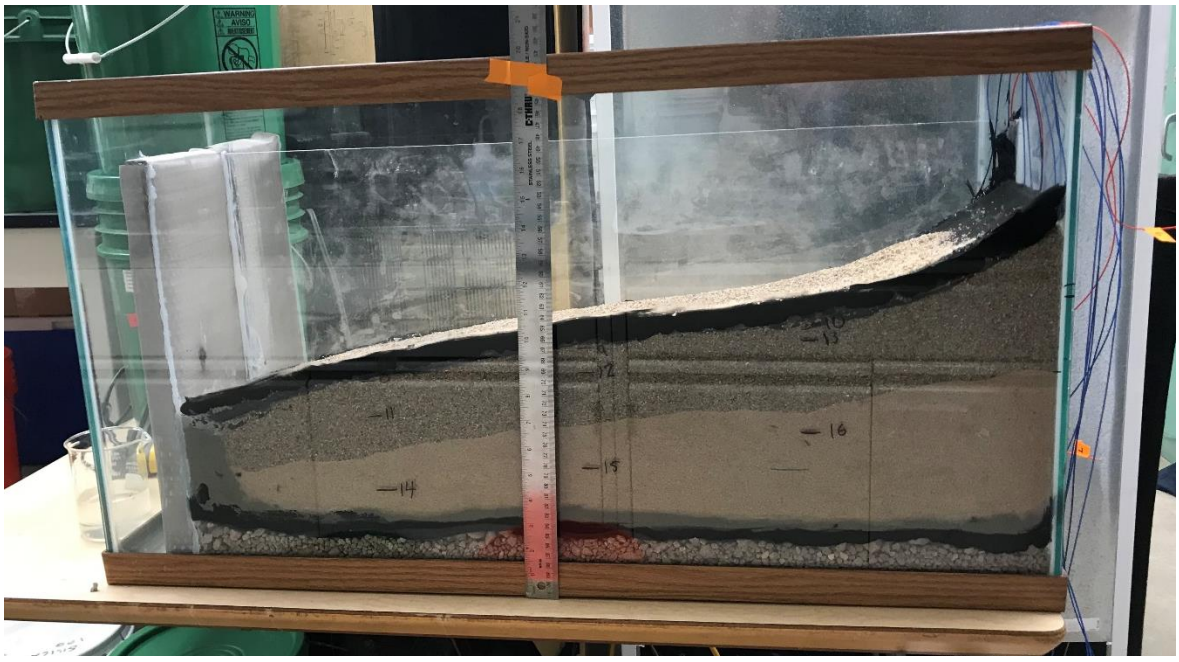

Figure A19. Photo of fine sand, coarse sand, and GDL installed in sand tank OBB.

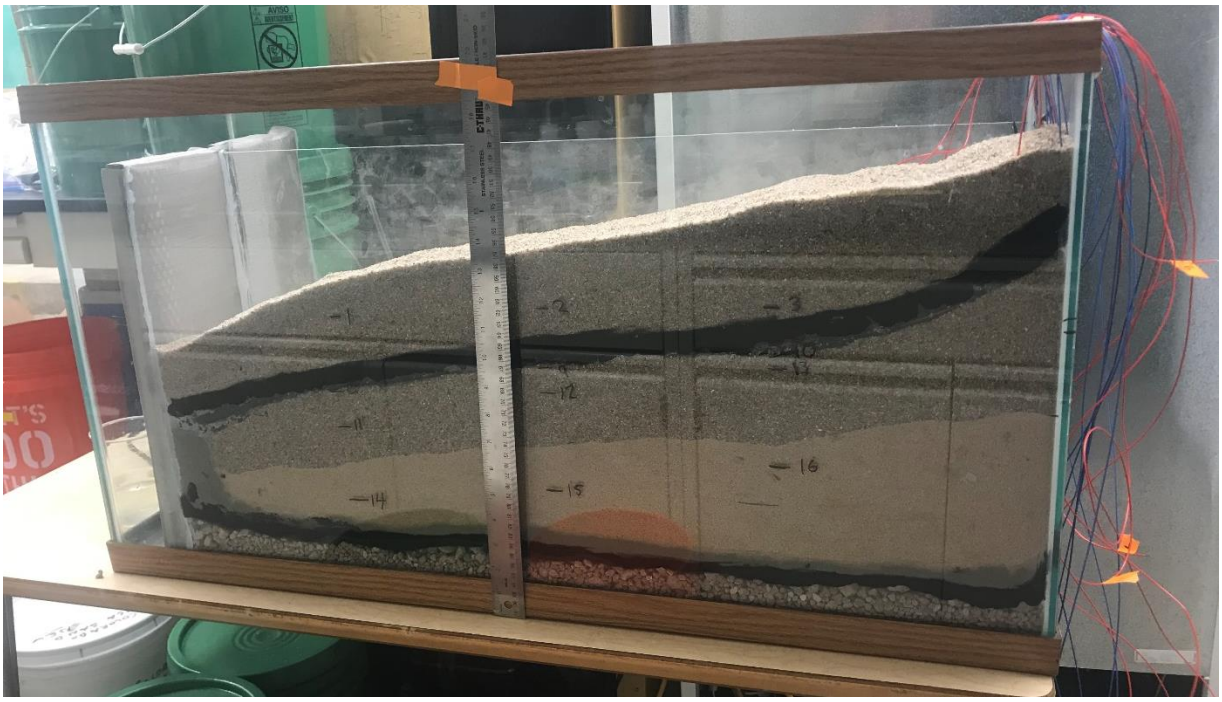

Figure A20. Photo of the completed sand tank OBB setup.

C3. Field OBB Monitoring Photos

Figure A21. Photo of field OBB site.

Figure A22. Photo of field OBB cofferdam.

Figure A23. Photo of the inside of the field OBB electrical enclosure.